Journal of Physics: Photonics

OPEN ACCESS

RECEIVED
9 June 2025

REVISED
1 August 2025

ACCEPTED FOR PUBLICATION
25 September 2025

PUBLISHED
7 October 2025

PERSPECTIVE

Chip-scale quantum sensors based on an integrated silicon carbide photonic platform

S Castelletto[1,*] and A Boretti[2]

[1] School of Engineering, RMIT University, Melbourne, Victoria 3001, Australia
[2] Independent Scientist, Wellington, New Zealand
[*] Author to whom any correspondence should be addressed.

E-mail: stefania.castelletto@rmit.edu.au

Keywords: silicon carbide, quantum sensors, integrated photonics, color centers, chip-scale, nano-sensing

Abstract

This review provides a forward-looking perspective on chip-scale quantum sensors based on integrated silicon carbide (SiC) photonic platforms. Although SiC quantum sensors, which utilize atomic point defects such as silicon vacancies and divacancies, are powerful tools for nanosensing, their performance in bulk-material configurations is often limited by factors such as poor photon collection and inefficient optical control. The novelty of this work lies in its focused analysis of how SiC photonic integration-leveraging components such as as waveguides, resonators, and metasurfaces can overcome these fundamental limitations. We explore how these integrated platforms enhance light-matter interactions, boost readout fidelity, and enable precise control over quantum states, providing a direct pathway to surpass the sensitivity of current bulk-material sensors. By synthesizing recent breakthroughs in SiC photonics with advances in materials science and quantum control, we outline a scalable road-map for developing high-performance, wafer-deployable quantum sensing systems for applications ranging from biomedical imaging to navigation in harsh environments.

1. Introduction

Quantum sensors are revolutionizing metrology, offering unprecedented sensitivity for detecting a wide range of physical quantities at the nanoscale, including magnetic fields, temperature, electric fields, and strain [1, 2]. These devices exploit quantum coherence and spin-dependent transitions to achieve measurements beyond classical limits, enabling breakthroughs in both fundamental science and applied technology. Among various platforms, point defects-based solid state quantum sensors in wide bandgap semiconductors, particularly color centers, have attracted significant attention due to their robust quantum coherence and their potential for miniaturization and operation in diverse environments from cryogenic to high temperature [3]. Their atomic-scale nature allows for nanoscale spatial resolution, while optical addressability enables noninvasive readout in complex environments.

Silicon carbide (SiC) is emerging as a compelling material for these sensors, offering advantages over diamond, such as wafer-scale fabrication, mature micro- and nano-fabrication techniques, available micro-electronics, compatibility with existing silicon technology, and high-temperature operation [4–6]. As a commercially available semiconductor, SiC bridges the gap between industrial scalability and quantum performance, making it uniquely suited for scalable quantum technologies when real-world applications are expected. Intrinsic point defects in SiC, such as silicon vacancy (V_{Si}^{-}) and divacancy ($V_{Si}V_{C}^{0}$), exhibit spin-dependent fluorescence in the near-infrared region to near telecom, making them suitable for deep tissue sensing and imaging in biomedical applications [7]. These defects combine long spin coherence times with efficient optical spin initialization and readout, even at ambient conditions.

Harnessing the quantum properties of these SiC color centers enables highly sensitive detection of magnetic fields and temperature, opening avenues for single-molecule sensing and advanced nano-metrology in harsh conditions [8]. Such capabilities are particularly valuable for applications in extreme

environments, including high-temperature industrial processes or *in vivo* biological sensing. Although significant progress has been made in SiC quantum sensing, recent work demonstrating advanced protocols such as the use of duplex qubits for enhanced performance [9], integrating these sensors with nanophotonics and nanoelectronics on-chip is crucial to improve signal collection, improve performance, and realize scalable, chip-based quantum systems with high spatial resolution [10, 11]. Photonic integration not only boosts sensitivity but also paves the way for multiplexed sensor arrays and hybrid quantum systems. Furthermore, the development of integrated sensor arrays opens up future possibilities for applying advanced computational techniques, such as quantum machine learning, to process complex multisensor data in real time [12].

This review analyzes the potential of integrated silicon carbide photonic platforms to advance chip-scale quantum sensing. Focusing on silicon vacancy and divacancy centers for magnetic field detection, it outlines key strategies and steps toward wafer-scale deployment [13]. By combining SiC's quantum defects with advanced photonic engineering, the goal is to develop practical high-performance sensors for applications ranging from fundamental physics to industrial monitoring and biomedical diagnostics.

2. Solid-state spin defects for magnetometry

Solid-state defects have seen rapid development in the past two decades because of their unique properties, which could offer a promising path toward scalable implementation of quantum information processing. In the field of quantum sensing, a few prominent examples are the nitrogen vacancy (NV) in diamond and the silicon vacancy or divacancy (V_{Si}^{-} or $V_{Si}V_{C}^{0}$) in SiC, both of which have been employed for room temperature magnetometry with a small sensing volume compared to the NV in diamond. These magnetometers belong to the category of optically pumped magnetometers (OPMs), which can operate at room temperature. Specifically, diamond and SiC can have high spatial resolution and can operate in large background fields (Earth's magnetic field), with SiC being more suitable for harsh environment operations at high temperature.

The magnetometer's figure of merit is the magnetic sensitivity, defined as the minimal magnetic field that can be detected by the sensor within a given measurement time. We will use this figure of merit in this manuscript to benchmark current magnetometer demonstrations performance. In addition, the sensing volume influences the sensitivity, and generally solid-state spin sensors in the ensemble are aimed at sensing volume of (10^{-12} m^3) using bulk materials [14]. By increasing the sensing volume, the number of interrogated spin sensors increases, and thus the sensitivity increases, while the spatial resolution reduces (see figure 1). There is a trade-off on these figures of merit depending on the desired use or applications. Larger sensing volume quantum sensors are desirable for applications such as magnetoencephalography for large-scale object (mm) sensing, while single spin sensors are more applicable to the investigation of molecular structures from micrometer to subnanometric scales [15]. However, increasing the sensitivity of ensemble solid state spin magnetometry such as diamond and SiC, by increasing the sensing volume, is limited by technical challenges such as achieving a uniform number of spin sensors across the volume with an efficient optical/microwave interrogation, requiring generally high power and ultimately deteriorating the spin properties due to dipolar interactions. On the other hand, photonics allows efficient use of micro- and nanoscale sensing volume and resolution, preventing the improvement of sensitivity by increasing the number of spin sensors. Photonics relies on achieving high-fidelity read-out of the spins within the confined volume to enhance sensitivity, maintaining high spatial resolution [16].

In this paper, we will outline various nanophotonic approaches to increase the sensitivity of optical spin defects quantum sensors in SiC with nano and microscale sensing volume, maintaining high spatial resolution up to sub-nanometric resolution.

To date, NV in diamond and the V_{Si}^{-} V2 line (917 nm) in 4 H-SiC quantum sensors magnetometry demonstrations have achieved sensitivities of the order of pT/$\sqrt{\text{Hz}}$ [17] and nT/$\sqrt{\text{Hz}}$ [8, 18], respectively.

Quantum sensing based on solid state spins requires long spin coherence times for higher sensitivity, which depends on the environment and can be controlled using spin manipulation mechanisms [3]. The spin coherence is distinguished in two main components: the inhomogeneous dephasing time T_2^*, which is intrinsic to the spin qubit, and the homogeneous dephasing time T_2. In diamond and SiC spin color centers, the electron spin T_2^* and T_2 are around a few hundreds of microseconds and few milliseconds [3], respectively even at room temperature, in the best material conditions, as we will discuss in the following sections. Other parameters are also relevant for the sensitivity enhancement based on the read-out method used.

In the following we will mainly focus on optical spin read-out, as it has been the most studied so far and focus on DC magnetometry based on optical detected magnetic resonance (ODMR).

This sensitivity of solid-state defects magnetometer depends on the measurement protocol utilized, the read-out methods, the number of solid-state defect sensors in the sampling material volume, the material properties such as isotopic purification, doping, centerges, and non-radiative recombination traps, and

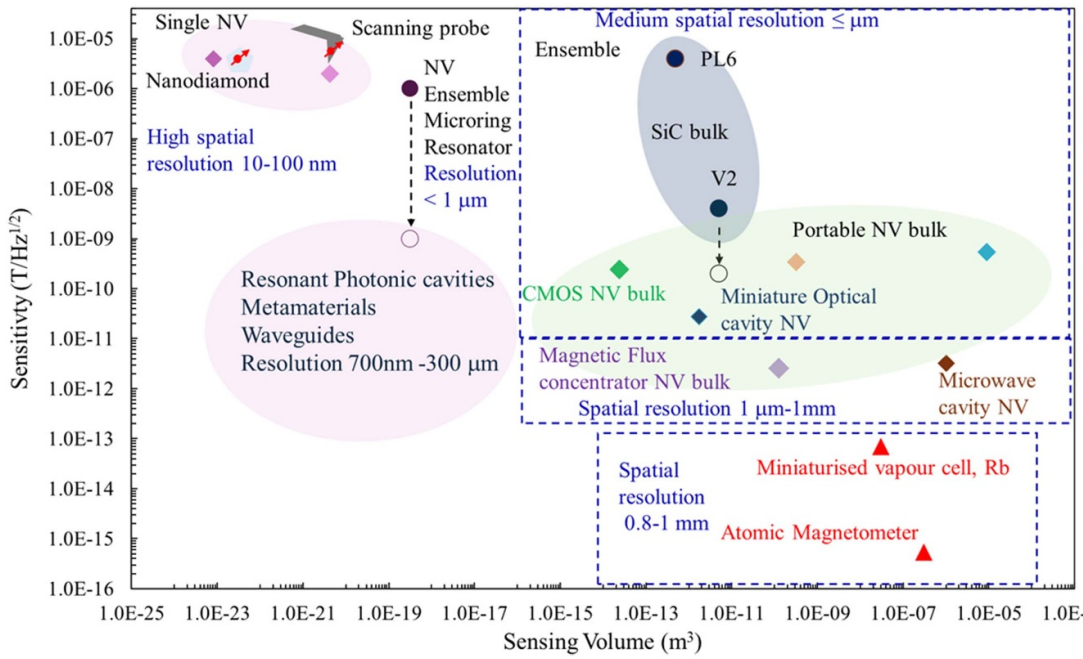

Figure 1. Comparison of magnetic field sensitivity versus sensing volume for various quantum sensing technologies. The plot includes data for atomic magnetometers, diamond NV centers (in bulk, nanodiamond, and integrated systems), and SiC color centers (V2 and divacancy). The gray shaded area highlights the projected performance improvements for SiC sensors enabled by integrated photonic structures such as resonant cavities, metasurfaces, and waveguides. The spatial resolution for different sensor types is also indicated. Data sourced from [8, 19–31].

finally on the photons collection efficiency (CE) and Purcell's enhancement of the emission of the solid-state sensors [14]. The reported sensitivity is still several orders of magnitude below the state of the art of other quantum sensors such as superconducting quantum interference devices (SQUIDs) and Alkali atom ensembles in vapor cells ($< \mathrm{fT}/\sqrt{\mathrm{Hz}}$) [15] (see figure 1). The current sensitivity of room-temperature OPMs based on atomic vapor is reported in [30, 31], the authors report sensitivities approaching 0.54 $\mathrm{fT}/\sqrt{\mathrm{Hz}}$, achieved with a very large sensing volume of 0.3 cm^3. More typical, practical atomic magnetometers, as reviewed by [32], tend to be in the 1–5 $\mathrm{fT}/\sqrt{\mathrm{Hz}}$ range. SQUIDs require a bulky and costly infrastructure including cryogenic cooling. Hall and tunnel magnetoresistance sensors are widely spread in consumers' electronic devices, e.g. smartphones, with a detection limit typically 1 $\mathrm{nT}/\sqrt{\mathrm{Hz}}$. These magnetometers are generally applied for large scale sensing.

There is a need to improve the sensitivity in diamond to the $\mathrm{fT}/\sqrt{\mathrm{Hz}}$ range for small and large sensing volumes, and in SiC to reach diamond level and go beyond, but also to achieve parallel quantum sensing and larger integration.

The existing solid-state defect-based magnetometry mainly on the diamond and emerging in SiC [6, 14], has the advantage of room temperature operation, can be miniaturized, and can operate in large background fields. However, they predominantly rely upon discrete and bulk crystal and optical components, which suffer from technical bottlenecks such as low photon collection/detection efficiency due to excitation and collection from the top of the sensor and limited optical/microwave (MW)/radiofrequency (RF) access and controls in the vicinity of the solid-state defects, in addition to inefficient excitation. Using bulk diamond with large ensemble of NV centers the sensitivity is increased as well as the sensing volume (figure 2). To build compact, practical, and scalable sensors for applications such as, for instance, in vehicle and biomedical systems, diamond sensors are miniaturized by combining optical fibers and complementary metal–oxide–semiconductor (CMOS) architectures, as recently reviewed in the perspective of [33]. Integrating a bulk diamond and the essential components for NV control and measurement such as microwave generator, optical filter, and photodetector, in a $200 \times 200\ \mu\mathrm{m}$ footprint using standard CMOS technology, quantum magnetometry was demonstrated with a sensitivity of 32.1 $\mu\mathrm{T}/\sqrt{\mathrm{Hz}}$ [34]. When miniaturized their sensitivity drops at the best realization to levels of 344 $\mathrm{pT}/\sqrt{\mathrm{Hz}}$ [25] for a fiber integrated with bulk diamond (sensing volume 0.32 mm^3) to 250 $\mathrm{nT}/\sqrt{\mathrm{Hz}}$ for the CMOS-NV sensor prototype $300 \times 80\ \mu\mathrm{m}^2$ area [27], depending on the sensing volume. Using magnetic flux concentrators and NV bulk diamond portable miniaturized magnetometer has reached sub-$\mathrm{nT}/\sqrt{\mathrm{Hz}}$ [26]. However, these demonstrations tend to rely on bulk optics, which are typically limited to scales of several centimeters. The

best miniaturized NV-diamond fiber magnetometer relies on the utilization of bulk diamond material [25]. Another approach to improve the sensitivity of diamond magnetometers is based on optimizing laser excitation and absorption for example using a high-finesse bulk optical cavity combined with pump-probe experiments, it significantly enhances the stimulated emission or absorption by the color centers, yielding in diamond an ODMR contrast for NV of over 42% , with a sensitivity of 7.5 pT/$\sqrt{\text{Hz}}$ [35], while similar miniaturized cavities can yield sensitivity of 28 pT/$\sqrt{\text{Hz}}$ [28]. Similarly, using strong coupling to a dielectric microwave cavity could overcome the optical photon shot noise limitations of conventional fluorescence readout and provide sensitivity of magnetic sensing of 3.2 pT/$\sqrt{\text{Hz}}$ [29].

While similar miniaturization can also be applied to bulk silicon carbide, more quantum sensor integration design directly in the material/device, incorporating key optical and optoelectronic components, is necessary to push this technology to the next level of development for future deployment in real-world applications requiring real time diagnostics and in-situ monitoring [33]. For example, one approach is to integrate sensor devices on-chip, based on recent advances in photonic integration in quantum photonic information and computing processing [36, 37]. While diamond-based magnetometry is very advanced and in some cases can be more practical than SQUIDs, which require cryogenic temperature, the difficulty to achieve high sensitivity via miniaturization, mainly suffers from the lack of diamond itself CMOS-microelectronics compatibility and lack of wafer scale diamond on insulator photonics, for its broader and actual sensor integration deployment. One step in this direction has been to demonstrate quantum sensing based on a large ensemble of NV centers in diamond small Q-factor (≈1000) microring resonators [22], where the ODMR contrast reached 25%, the maximum so far detected for ensemble of NVs close to the theoretical value for single NV of 30%, reaching sensitivity of 1 μT/$\sqrt{\text{Hz}}$ (1 nT/$\sqrt{\text{Hz}}$ theoretical).

A primary limitation in solid-state spin-defect quantum sensing is achieving robust and scalable device integration. A promising solution is the silicon-carbide-on-insulator (SiCOI) integrated photonics platform, which offers distinct advantages for creating chip-scale quantum sensors based on silicon vacancies and divacancies. SiC is an industrially mature semiconductor, with current wafer scale production already reaching 'quantum grade' readiness. Being CMOS compatible, SiC enjoys fabrication scalability, controllable p- and n-doping, and the capability of integrating optoelectronic (photodetectors) and photonic components for linear and nonlinear light-matter interactions. SiCOI furthermore offers a powerful platform for photonic integration, where implementation of large-scale circuits for both leveraging light–matter interaction and on-chip photonic manipulation and processing can be achieved. Low-losses (2 dB cm^{-1}) and high uniformity thickness SiCOI fabrication methods have been optimized to achieve wafer scale fabrication processing using dopant-selective photo-electrochemical etching to leave an epitaxially defined intrinsic layer of high purity compatible with color center emission. Photonics fabricated in such SiCOI showed an high yield of optical elements [38].

3. Silicon vacancy

Among a variety of color centers hosted by the hexagonal 4 H-SiC, this review initially focuses on the negatively-centerged silicon vacancy (V_{Si}^-) as it is one of the most extensively studied spin defects for room-temperature quantum sensing applications in SiC. Its well-centeracterized properties make it an ideal case study for illustrating the principles of spin-based sensing and the potential benefits of photonic integration, before introducing other key defects such as the divacancy. Here we focus on the negatively-centerged silicon vacancy (V_{Si}^-) centers at the cubic lattice site, known as V2 line, which corresponds to a zero phonon line (ZPL) at 916.4 nm [39], spin $S = 3/2$ [40, 41] and with a Debye–Waller factor of 8%–9% [42], (see figure 2(a)). V2 has been a use case for room-temperature magnetic field sensing [43] using bulk irradiated hexagonal SiC with a high concentration of these color centers, more specifically the 4 H-SiC has been used, as also reviewed in [6]. The V2 line has been intensively investigated as a qubit spin-photon interface in the more recent years(V_{Si}^-) centers [40–42, 44–67]. The spin Hamiltonian of an $S = 3/2$ electron spin defect within a nuclear spin bath can be written as:

$$\hat{\mathcal{H}}_{spin} = g\ \mu_B \hat{\mathbf{S}} \cdot \mathbf{B_0} + D\left(\hat{\mathbf{S}}_z^2 - \frac{\hat{\mathbf{S}}\left(\hat{\mathbf{S}}+1\right)}{3}\right) + E\left(\hat{\mathbf{S}}_x^2 - \hat{\mathbf{S}}_y^2\right) + \sum_j \hat{\mathbf{S}}_i \cdot \mathbf{A_{ij}} \cdot \hat{\mathbf{I}}_j, \tag{1}$$

where g is the isotropic center specific Lande factor ($g = 2.0028$), μ_B is the Bohr magneton, $\mathbf{B_0}$ is the external magnetic field, D and E are the is the crystal field splitting tensors, accounting for the zero magnetic field splitting for the axial (along the spin polarization axis z) or the off-axis component of the spin defect operator $\hat{\mathbf{S}} = (\hat{\mathbf{S}_x}, \hat{\mathbf{S}_y}, \hat{\mathbf{S}_z})$, respectively. $\mathbf{A_{ij}}$ is the hyperfine tensor that describes the central spin coupling to many nuclear spins indexed by j with spin operators $\hat{\mathbf{I}}_j$. The first term represents the electron Zeeman

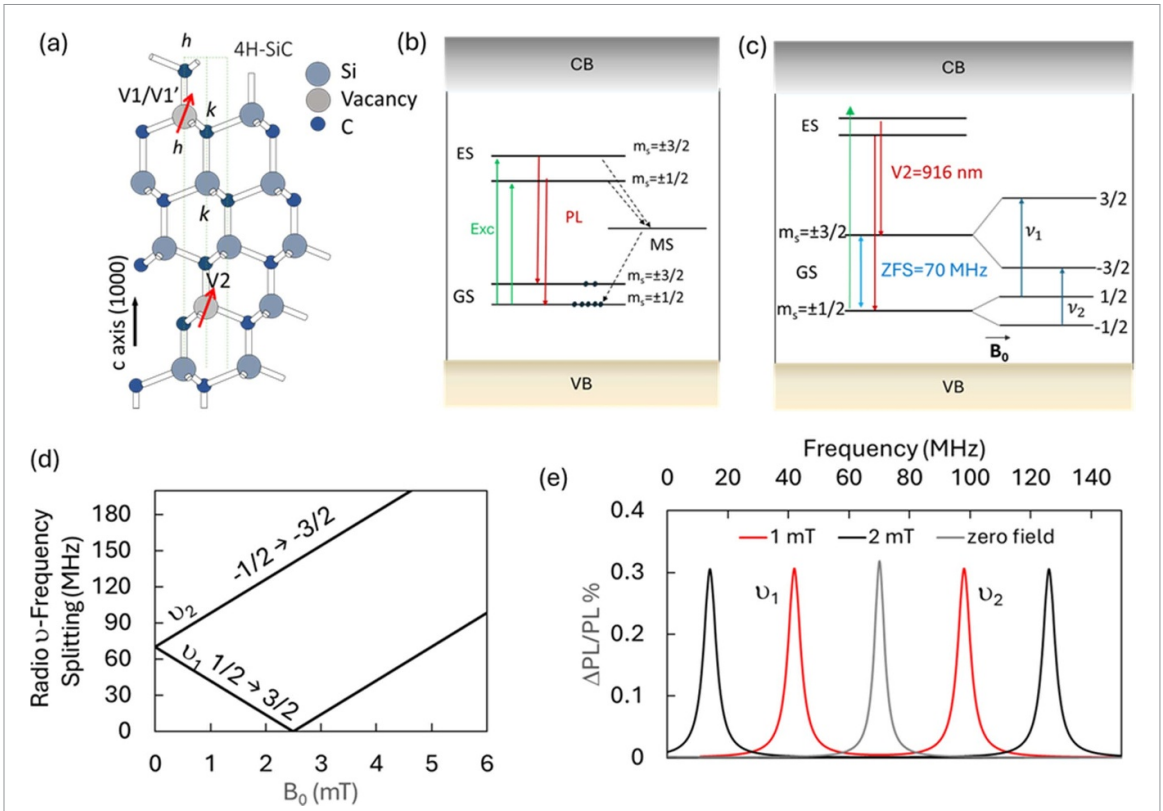

Figure 2. (a) Crystallographic sites of V1 and V2 centers in 4 H-SiC. (b) Simplified energy level diagram illustrating the optical spin polarization cycle of the V_{Si} defect. Off-resonant optical excitation populates the excited state (ES), leading to photoluminescence (PL). A non-radiative intersystem crossing (ISC) to a metastable state (MS) preferentially populates the $m_s = \pm 1/2$ spin sublevels in the ground state (GS). (c) V2 center energy levels showing spin transitions relevant for magnetometry. (d) Zeeman splitting of spin levels under an applied magnetic field. (e) Simulated CW-ODMR spectra showing the change in PL at zero field and in the presence of a magnetic field. This is one of the the simplest and main mechanism for quantum sensing in SiC.

interaction with the external magnetic field $\mathbf{B_0}$, the second and third terms are the axial and off-axis zero-field splitting (ZFS), and the fourth term is the hyperfine interaction. Other spin interactions such as the quadrupole and the nuclear Zeeman interactions, are also involved in the spin centers interaction with the nuclear spin environment.

For the V_{Si} the optical spin polarization is enabled by the intersystem crossing (ISC) with a combination of optical driving, spin–orbit coupling (SOC), and interaction with vibrational modes [58] (see figures 2(b) and (c)).

Optical pumping results in a preferential population of either the $m_s = \pm 3/2$ or $m_s = \pm 1/2$ states, depending on SiC polytype and the V_{Si} crystallographic site.

Specifically, for the 4 H-SiC polytype V2 line, it was shown that the radiative relaxation giving rise to V2 emission from the excited state (ES) to the ground state (GS) is a spin-conserving process, e.g. the electrons with a spin $m_s = \pm 1/2(\pm 3/2)$ in the ES will decay only to the $m_s = \pm 1/2(\pm 3/2)$ level in the GS [56]. However, there is a competing non-radiative relaxation process mediated by a metastable (MS) or shelving state with $m_s = \pm 1/2$, located between the ES and the GS. In this process, electrons in the ES from $m_s = \pm 1/2(\pm 3/2)$ would decay first to the MS, and finally to $m_s = \pm 1/2$ level in the GS, due to the SOC, electrons with spin $m_s = \pm 3/2$ experience spin flip decay into the MS. This process called ISC produces a population imbalance at the GS after multiple optical excitations (figure 2(b)).

The ZFS frequency (ν_{ZFS}) of the V_{Si}^- V2 is $2D = 70$ MHz. In the presence of an axial magnetic field at room temperature, $\mathbf{B_0}$, along the c-axis, which is also the V2 crystallographic axis, the Zeeman frequency splitting varies linearly with the magnetic field, for small magnetic fields as $\nu = \nu_{ZFS} \pm g\mu_B/hB_0$. $g\mu_B/h = 28.032\ \mathrm{MHz\,mT^{-1}}$ is the electron gyromagnetic ratio. A MW/RF excitation provides an induced transition between magnetic field-related Zeeman sublevels of the V2 with $\Delta m_s = \pm 1$ (figure 2(c)). The resonance frequencies of the RF excitation are linearly dependent on the external on-axis magnetic field for low values of the magnetic field, $\mathbf{B_0}$.

Continuous-wave optically detected magnetic resonance (CW-ODMR) is one of the fundamental magnetic field sensing techniques in SiC and diamond defects, and even if not the most sensitive, however, its

simplicity surpasses other methods based on pulsed MW/RF sequences. This is described in the following and represented in figures 2(d) and (e). It is based on changing the fluorescence intensity when an applied RF field is resonant with a ground-state spin transition, typically of magnetic quantum number $m_s = \pm 1/2 \leftrightarrow m_s = \pm 3/2$. Here laser excitation continuously polarizes the V_{Si}^- centers into the less fluorescent $m_s = \pm 1/2$ GS, while the RF-tuned near resonance with one of the $m_s = \pm 1/2 \leftrightarrow m_s = \pm 3/2$ transitions drive the V_{Si}^- population into the more fluorescent $m_s = \pm 3/2$ state (enhancing the emitted light). A change in the local magnetic field shifts the resonance feature with respect to the RF, causing a change in the detected fluorescence. The ground-state transition energies are a function of the ambient magnetic field through the Zeeman effect. Thus, the ambient magnetic field is measured through the ground-state transition energy change when it is applied the RF frequency, through a change in the photoluminescence intensity (figures 2(d) and (e)). By scanning the value of the axial magnetic field, two sets of ODMR signals with linear behavior can be used for quantum sensing (figure 2(e)). In the simplest CW-ODMR implementation, the RF frequency is swept across the entire V_{Si}^- resonance spectrum, allowing all resonance line centers to be determined.

4. Modified divacancy

The divacancy and modified divacancy centers in SiC are the other most studied centers, that also hold promises for their implementation in quantum sensing and as spin-photon interface, and can operate also at room temperature. Another prominent color centers in SiC such as the NV [6] is only mentioned here as fewer publications are focused on quantum sensing; while the vanadium in SiC [11] is considered more promising for quantum communication and computing due to low temperature operation. The divacancy centers in SiC ($V_{Si}V_C^0$, $g = 2.0030$) [4, 68–73], are an uncenterged complex consisting of neighboring C and Si vacancies and have a residual $S = 1$. They have been studied for single photon emission and single spin manipulation owing to their long spin coherence times [73] and can be optically [69] and electrically [74] controlled to reduce the quantum electric and magnetic noise, showing record minutes long spin coherence [75], therefore are posed to achieve disruptive opportunities in quantum sensing, quantum network and long distance entanglement distribution [76]. There are four types of confirmed divacancies PL1-PL4, with PL1, PL2 (1130 nm) along the c-axis, PL3, PL4 (1078 nm) in the basal plane [68, 69]. For S = 1 the spin the Hamiltonian reduces to [69]

$$\hat{\mathcal{H}}_{spin} = g\ \mu_B \hat{\mathbf{S}} \cdot \mathbf{B_0} + D\hat{\mathbf{S}}_z^2 + E\left(\hat{\mathbf{S}}_x^2 - \hat{\mathbf{S}}_y^2\right) + \sum_j \hat{\mathbf{S}}_i \cdot \mathbf{A_{ij}} \cdot \hat{\mathbf{I}}_j. \tag{2}$$

These Hamiltonians form the theoretical foundation for spin-based quantum sensing. The crucial term for magnetometry is the Zeeman interaction, $g\mu_B \hat{\mathbf{S}} \cdot \mathbf{B_0}$, which describes the energy shift of the spin sublevels in proportion to an external magnetic field $\mathbf{B_0}$. ODMR measures this shift by monitoring the defect's fluorescence while sweeping a MW frequency to drive transitions between the spin states. A change in the magnetic field alters the resonance frequency, which is detected as a change in photoluminescence. The sensitivity of this measurement, as formulated in align (3), is directly linked to the Hamiltonian's parameters. Specifically, the gyromagnetic ratio, $g\mu_B/h$, dictates the magnitude of the frequency shift per unit of magnetic field, thus fundamentally connecting the sensor's response to the intrinsic quantum properties of the spin defect.

For $V_{Si}V_C^0$ the c-axis defects have $E = 0$ while the lower-symmetry basal defects have significant values for E [77, 78]. In addition so called 'modified divacancy' were discovered such as PL5 (1041.9 nm) and PL7 assigned as basal [4, 68, 69] and PL6 (1037.7 nm) assigned along the c-axis. Recently by electron paramagnetic resonance methods, it was determined that PL5 and PL6 are slightly deviated from axial symmetry [80]. For PL5 the zero field splitting $D = 1.328$ GHz and $E = 13$ MHz, while for PL6 $D = 1.357$ GHz and $E = 6$ MHz [80]. Unlike the usual divacancy PL1–PL4 centers, which are not detected at room temperature and exhibit PL quenching [81] requiring re-pumping, the PL5–PL7 centers have stable PL emissions and high brightness single photon emission at room temperature [68, 82], with spin coherent control even above 550 K and temperature sensing up to 450 K have been demonstrated [83, 84]. PL6 can be a single center with 150 kcounts s^{-1} at room temperature, up to 460 kcounts s^{-1} [85], without any photonic structure. They can be created by C-ions implantation [68, 82], electron irradiation [80], focused helium ion beam (He FIB) (figure 3(a)) [79], and direct laser writing [86]. These defects show much higher ODMR contrast even at room temperature than the other divacancy [82] and comparable/higher of the single NV center in diamond, as shown in figures 3(b) and (c) for the ODMR of PL6 and PL4 (the change of PL intensity under resonant conditions is up to 30% for PL6 [82]). The PL6 has been studied under resonant excitation showing two transitions from the ground to the ES ($E_{X,Y}$), shown in figure 3(d). The effect of PL6

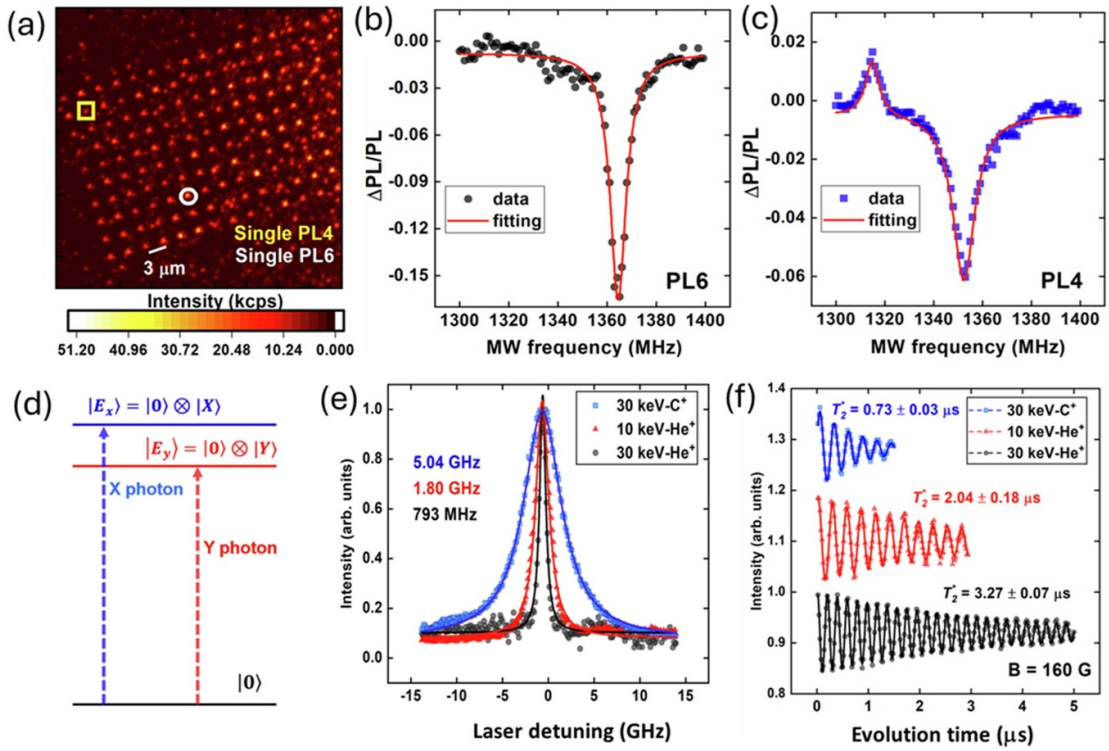

Figure 3. (a) Confocal fluorescence scan showing an array of divacancies created by a focused He ion beam. Individual PL4 and PL6 centers are identified. (b), (c) Low-temperature ODMR spectra of single PL6 and PL4 centers, respectively. (d) Energy level diagram for the PL6 center, showing two optically addressable transitions with orthogonal polarizations. (e) Photoluminescence excitation (PLE) spectra of a single PL6 center, highlighting the E_y transition. (f) Ramsey interference fringes for a single PL6 center, demonstrating coherent spin manipulation. Reproduced from [79], with permission from Springer Nature.

fabrication approaches on the spectral broadening and spin dephasing T_2^* is shown in figures 3(e) and (f). However currently their identification is still debated. They were initially assigned theoretically to divacancy located at or near Frank-type stacking faults [87], where a band gap narrowing effect due to stacking faults, could provide robustness against photoionization and room temperature stability. This model is not experimentally confirmed [80] and by correlating stacking faults imaging with single PL5-6 detection, it is shown that these modified divacancy can be present outside of stacking faults [85]. Since many different kinds of *c*-axis and *basal*-type divacancy exist in a divacancy ensemble without an external magnetic field, several ODMR resonances from these divacancy overlap. Therefore, a relatively large bias magnetic field must be used. Due to the divacancy lack of trigonal pyramidal symmetry, only two resonance frequencies can be detected in the ODMR spectrum corresponding to $m_s = 0 \leftrightarrow m_s = \pm 1$, these frequencies are at zero field: for PL6 1.3514 GHz, for PL5 there are two resonances at 1.3757 GHz and 1.3437 GHz, for PL7 the resonance is at 1.333 GHz.

5. Magnetic field sensitivity based on CW ODMR

The magnetic field sensitivity is limited by shot noise, and it is given by [18]

$$\eta_{\mathrm{CW-ODMR}} = \frac{4\sqrt{2}}{3\sqrt{3}} \frac{h}{g\mu_{\mathrm{B}}} \frac{\Delta\nu}{C_{\mathrm{CW-ODMR}}\sqrt{R}}, \tag{3}$$

where $\Delta\nu$ is the full width at half maximum (FWHM) of the ODMR linewidth, $C_{\mathrm{CW-ODMR}} = |\Delta PL/PL|$ is the ODMR normalized fluorescence contrast, due to the PL variation in presence and without presence of the MW/RF excitation and R is the rate of detected/collected photons from the defect ensemble. R is dependent on the CE, CE, and in the number of spin quantum sensors interrogated in the material, N, as this directly related with the interrogated volumes or the spin sensors density. While N can be theoretically increased, in practice there are limitations on how many spin sensors can be created in a small volume, as they interact due to their close proximity inducing dephasing from dipolar coupling and thus reducing the T_2^*; increasing the detection volume to accommodate more spins with the same density can be impractical due to high excitation power required and non-uniform MW and magnetic field interaction as well as

non-uniform spin sensors over a larger volume. The pre-factor in align (3) originates from the steepest slope of the ODMR resonance line shape when assuming a Lorentzian resonance profile. The theoretical sensitivity can be optimized by factors depending on the specific spin defects ensemble properties and the operating experimental conditions such as:

$$\eta_{\mathrm{CW-ODMR}} = \frac{4\sqrt{2}}{3\sqrt{3}} \frac{h}{g\mu_{\mathrm{B}}} \frac{\Delta\nu\left(\Omega_{\mathrm{R}}\left(W\right), s\right)}{C_{\mathrm{CW-ODMR}}\left(\Omega_{\mathrm{R}}\left(W\right), s\right)\sqrt{R\left(P_{\mathrm{opt}}\right)}}, \tag{4}$$

where P_{opt} is the optical excitation power, W is the MW or radio-frequency power. The $\Delta\nu$ and the $C_{\mathrm{CW-ODMR}}$ in practice depend on the Rabi frequency, $\Omega_{\mathrm{R}}(W) \propto \sqrt{W}$, and the ratio $s = \frac{P_{\mathrm{opt}}}{P_{\mathrm{sat}}}$, between the optical power used and optical saturation power, P_{sat} [24]. Further the detected/collected photon rate R depends on the photonic environment, as it will be discussed in sections 6.5, 6.6 and 6.10.

6. Sensitivity optimization strategies

Improving the sensitivity beyond the state of the art essentially hinges on the following factors based on align (3): increasing $C_{\mathrm{CW-ODMR}}$ and reducing $\Delta\nu$, material purification and defects fabrication improvement, extension of the coherence time T_2^*, increase of the the photon v CE and photon emission rate out of the material, reducing volume and power of the optical excitation, control the centerge state of the color center and its spectral emission stabilization by tailoring the optical excitation.

In the following we discuss the optimization of all the above factors to improve sensitivity, in particular focusing on the role of photonics for future endeavors. We envision the development of chip-scale magnetometry systems that combine ODMR methods with a range of photonic integration components to significantly improve some of these factors, in particular optical and MW excitation and absorption, CE and fluorescence emission enhancement.

6.1. ODMR contrast and spectra

To improve the sensitivity, the ODMR contrast and spectra are to be optimized. The ODMR signal optical contrast, $C_{\mathrm{CW-ODMR}}$, should be as high as possible to facilitate optical readout and enable practical implementations. $C_{\mathrm{CW-ODMR}}$ is a direct measure of the quality of the spin-photon interface of the defect reduced by the existence of non-radiative pathways such as the ISC, which are required to enable optical spin polarization in the GS. Given the strong ISC in V_{Si}, the resulting optical contrast is below 0.4% (at off-resonant excitation and without any contrast-enhancing techniques), which is low in comparison to the contrast of other defects such as the NV center in diamond or the PL5/PL6 [7, 60, 82].

The ODMR contrast can be greatly enhanced of more than one order of magnitude by using resonant and non-resonant nanophotonics as it will be discussed in sections 6.5 and 6.6.

The ODMR linewidth,$\Delta\nu$, is a result of competing spin-spin interaction mechanisms that result in a broadened or narrowed spectrum. Decoherence of the vacancy spins caused by the dipolar interaction with fluctuating nearby nuclear or electron spins broadens the ODMR linewidth. This so-called inhomogeneous broadening is a result of the spatial variation of the effective magnetic field due to the dipolar contribution from the spin bath. A spatially-varying magnetic field will result in a superposition of spin resonances, which broadens the ODMR linewidth. $\Delta\nu$ is fundamentally limited by the inhomogeneous spin dephasing time, T_2^* [14], and it is $\Delta\nu \propto 1/T_2^*$, which in the case of SiC is due to the fluctuating magnetic field from the nuclear-spin-carrying isotopes of the host crystal such as ^{29}Si and ^{13}C in addition to other electron spins due to other defects or nitrogen interstitial associated to doping [88]. The linewidth $\Delta\nu$ can also be broadened by the RF power being delivered to the sample in the ODMR experiment [89]. We discuss approaches to reduce the broadening of the ODMR linewidth and improve the ODMR contrast.

6.2. Coherence time improvement via material purification, thermal annealing and spin defects fabrication

Careful material purity control and spin-defect fabrications are necessary to reduce the impact of these sources of decoherence. Nuclear spin purification during growth is used in research laboratories to reduce nuclear spin decoherence [90]. One order of magnitude improvement of T_2^* for the V_{Si} was achieved by nuclear spin isotopic purification [91]. Post-irradiation optimal thermal treatment can be used to reduce the excess of other defects generation [92] such as the EH3 centers, a type of deep-level defect, located approximately 0.7 eV below the conduction band minimum band structure, introduced through ion implantation or neutron irradiation. EH3 centers are associated with silicon vacancies or defect complexes involving interstitial.

The coherence time and spin dephasing time for ensemble in isotopic purified SiC can be realistically improved, however more systematic approaches in color center fabrication, annealing, and surface defects quenching are needed; currently, only few studies have addressed the improvement of the spin coherence in ensemble via defects engineering and design [93]. The suppression of undesired spin defects, that can be generated during fabrication and can quench both the emission and reduce the spin coherence, is still a challenge. Utilization of low nitrogen doping and low defect concentration in isotopically purified SiC wafers to obtain high-quality SiC epilayers, combined with annealing and quenching of electron-irradiated samples or direct laser writing of the silicon vacancy [94] and laser annealing [95], could improve the spin coherence time T_2 and the spin-read out fidelity. Ramsey interferometry for single He^+ implanted V2 centers have shown dephasing time $T_2^* = 34 \pm 4\,\mu$s [66], while using focused He-beam the spin-echo coherence was extended to 194 μs with 160 gauss magnetic field and $T_2^* = 3\,\mu$s for PL6 (figure 3) [79].

Spin defect fabrication methods are key to reducing decoherence [96, 97]. A factor of 10 improvements can be achieved in CW-ODMR simply by improving the fabrication methods using specific ions and the post-fabrication process [97, 98]. Using femtosecond laser written internal micro-optical structures on pre-existing V_{Si} in ensemble, 2.5 higher saturated fluorescence than untreated samples and 1.7 spin read out sensitivity enhancement was achieved [99]. It is expected that using laser writing [86, 100] or low mass He ions to create vacancies [98] could be beneficial for the fabrication of the qubits. It has been shown that using proton beam high concentrations of V_{Si} with higher ODMR contrast of 0.8% could be achieved [101].

Efforts in material purification, spin-qubits fabrication, and post-fabrication improvement are ongoing. These material process optimizations mostly benefit the sensitivity in magnetometry based on pulsed schemes as directly dependent on T_2^*, such as Ramsey methods, as described below.

In general, the key material/fabrication approaches to be sought after are to use methods less damaging to create qubits and fabricate nanostructures around them without reducing the spin coherence time, improving optical and MW fields, coupling efficiency with the qubits and improve the collection/detection efficiency. Nuclear spins purification to improve the coherence time is a less necessary approach for quantum sensing as the process makes the material more expensive and not scalable as not compatible with industrial processing.

6.3. RF and optical excitation power optimization

The CW-ODMR method suffers mainly from the RF and optical power used. The CW ODMR signal depends on the MW power W and the laser optical power, P_{opt} that is supplied to the sample. The maximum amplitude of the ODMR when in resonance has been determined as [43, 89]

$$A_R(W) \propto \frac{1}{1 + P_o/P_{\text{opt}}} \times \frac{1}{1 + W_o\left(P_{\text{opt}}\right)/W}, \tag{5}$$

where $P_o = \frac{1}{kT_1}$ is the centeracteristic optical power density, where k is a proportionality coefficient defining the spin-pumping rate $kP_{\text{opt}}n_{m_s=\pm1/2}$ from spin sublevels $m_s = \pm1/2$ to $m_s = \pm3/2$, with $n_{m_s=\pm1/2}$ the population of sublevels $m_s = \pm1/2$. T_1 is the spin-lattice relaxation time occurring after sublevels $m_s = \pm1/2$ are excited to $m_s = \pm3/2$. The centeracteristic MW power is determined to be

$$W_o\left(P_{\text{opt}}\right) = \frac{1 + P_{\text{opt}}/P_o}{\chi\left(\frac{g\mu_B}{\hbar}\right)^2 T_1 T_2^*}, \tag{6}$$

where χ is a coefficient related to the Q-factor of the RF resonator providing power $W = \frac{B_1^2}{\chi}$, with B_1 the radio frequency generated magnetic field. The FWHM of the ODMR resonance is determined as

$$\Delta\nu = \text{FWHM} = \frac{\hbar}{g\mu_B T_2^*} \times \sqrt{1 + \frac{W}{W_o\left(P_{\text{opt}}\right)}}, \tag{7}$$

and it is generally fit by a Lorentzian distribution.

For V_{Si} the high RF power is broadening the $\Delta\nu$, reducing the sensitivity, while high RF power improves the contrast $C_{\text{CW-ODMR}}$ [89] up to saturation of the transition. In figures 4(a) and (b) the effect of the RF power and optical power on the V2 magnetic field sensitivity for two differently annealed samples is shown, demonstrating that more than a factor of 10 sensitivity improvement can be achieved by careful optimization of the optical and RF power and of the annealing. It was found for the V_{Si} that the FWHM is essentially independent of the optical power and the contrast increases with the optical power [18]. An optimal MW power and optical power are expected to achieve the best sensitivity. Similarly, it was found for PL6 modified divacancy where the ODMR contrast and FWHM are determined for different optical power and Rabi

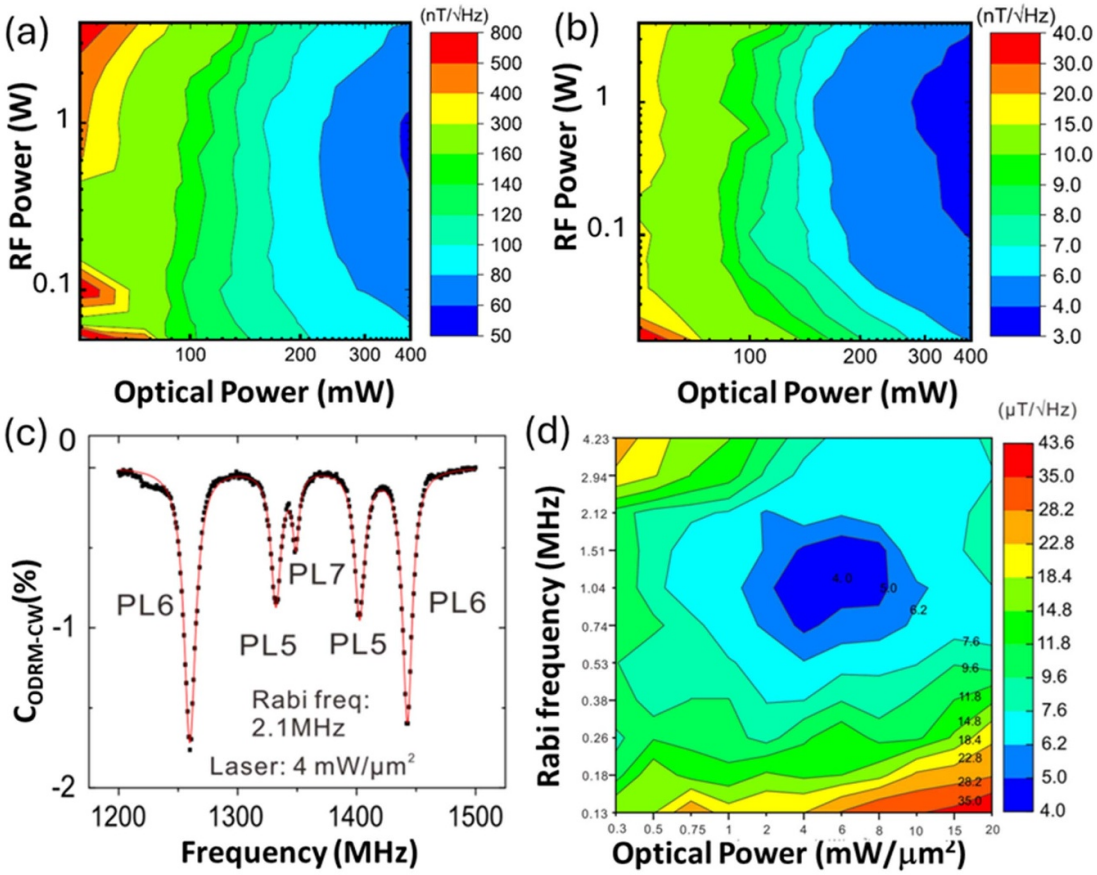

Figure 4. (a) and (b) Shot-noise sensitivity of an ensemble of V2 centers as a function of optical power for an annealed and a quenched SiC sample, respectively. (c) ODMR contrast for an ensemble of modified divacancies at a magnetic field of 3.25 mT. (d) Experimental magnetic field sensitivity for PL6 centers as a function of laser power and microwave-driven Rabi frequency. (a) and (b) Reprinted figure with permission from [18], Copyright (2021) by the American Physical Society. (c) and (d) Reprinted figure with permission from [102], Copyright (2020) by the American Physical Society.

frequency (figure 4(c)). The Rabi frequency $\Omega_R = \frac{g\mu_B}{\hbar} B_1 = \frac{g\mu_B}{\hbar}\sqrt{\chi W}$, where B_1 is the RF magnetic field, linearly increases as a function of the square root of the MW power, W [102], therefore optimal Rabi frequency should be used to optimize the contrast and the spectral broadening (figure 4(d)). It is found that higher laser power tends to reduce the contrast and $\Delta\nu$ is independent from the laser power or increase with laser power, while the ODMR contrast and FWHM increases with the Rabi frequency (higher MW power) [102]. The theoretical approach is also needed to guide the optimization of RF and laser power for SiC. Optimal optical and MW power using bulk components can improve the magnetic field sensing sensitivity by a factor of 10 [102]. Optimal CW-ODMR sensitivity is approximately achieved when optical excitation, MW drive, and T_2^* dephasing contribute roughly equally to the resonance linewidth. In this low-optical-intensity regime, the detected fluorescence rate per interrogated spin center is significantly low. It is therefore expected that improving the optical and MW excitation via photonics and integrated MW cavities will require less power as better excitation can be achieved.

6.4. Pulsed RF and optical excitation

The ODMR resonance broadening issues are not present in pulsed ODMR schemes at the expense of complexity, longer acquisition time, and higher optical and MW power. Pulsed approaches by themselves can improve the sensitivity of a factor of 10 as shown in the early days for NV in diamond [103] and the best sensitivity values for diamond were achieved with pulsed sequences, which are however generally more complex and require overhead time for initialization and read-out. The Ramsey pulse scheme is relevant for V2: after the optical initialization by a 30 μs laser pulse, which places the spin states $m_s = \pm 1/2$ in an equal mixture, an RF π pulse is applied to excite the spins from $-1/2 \rightarrow -3/2$ and create a population difference between 1/2 and –1/2 spins. A standard Ramsey sequence is run between 1/2 and –1/2 spins to have a free evolution decay for a time of 1/2 spins. A final RF π pulse is applied to excite the spins from $-1/2 \rightarrow -3/2$ and read out the population difference between 1/2 and –1/2. A benefit of this method is that the sensitivity is limited by the T_2^* of the transitions and is not affected by power broadening, as in the CW ODMR method.

Specifically, for the V2 center this method can utilize significantly longer coherence times of the $-1/2 \rightarrow 1/2$ transition. The shot-noise-limited in this case is given by [8],

$$\eta_{\text{Ramsey}} = \frac{\hbar}{g\mu_B \Delta m_s} \frac{1}{C_{\text{Ramsey}}\sqrt{N}e^{-(\tau/T_2^*)}} \frac{\sqrt{(t_I + \tau + t_R)}}{\tau}, \tag{8}$$

where Δm_s is the spin difference between the two states, C_{Ramsey} is the Ramsey-ODMR fluorescence contrast, N is the rate of collected/detected photons per pulse, τ is the free evolution time, and $t_{I,R}$ are the initialization and read-out time of the Ramsey sequence. This sensitivity is one order of magnitude better than $\eta_{CW-ODMR}$. The shot noise sensitivity for V2 is estimated for bulk optics as per the experiment [8] at 200 pT/$\sqrt{\text{Hz}}$.

6.5. Rate of the detected photons enhancement

The rate of the detected/collected photons $R \propto \text{CE} \cdot \text{QE} \cdot F_p$ from the defect ensemble is limited by the shelving time in the MS state or its quantum efficiency (QE) and is further reduced by the suboptimal CE of the emitted photons, even using a high numerical aperture (NA) objective, as it is usually done with bulk optics. CE is generally limited by the dipole orientation of the emitter in the crystal, providing a specific spatial emission pattern which is only in part collected. A substantial fraction of fluorescence that is radiated is also trapped inside the high-refractive-index diamond or SiC substrate ($n_{\text{diamond}} = 2.4$, $n_{\text{SiC}} = 2.6$) by total internal reflection, or radiated with a reduced effective numeral aperture. The emitter quantum efficiency is $QE = \frac{\gamma_{\text{rad}}}{\gamma_{\text{rad}} + \gamma_{\text{nonrad}}}$, where $\gamma_{\text{rad,nonrad}}$ are the radiative and non-radiative decay rates of the emitter, this last includes generally a non-radiative ISC state. In addition, the detected photon rate can be improved by engineering the center radiation emission by modifying the local density of states in the environment where it is radiating, thus accelerating the emission rate [104]. This is usually achieved with a photonic or plasmonic cavity. This emission rate modification is quantified by Purcell's enhancement $F_p = \frac{\gamma_{\text{nano}}}{\gamma_{\text{bulk}}} = \frac{\tau_{\text{bulk}}}{\tau_{\text{nano}}}$ [105], where $\gamma_{\text{nano,bulk}}$ are the emitters' radiative decay rates in the nanostructure or in the bulk, which are the inverse of the optical lifetime, $\tau_{\text{bulk/nano}}$. Thus, the Purcell's enhancement quantifies the ES's lifetime reduction. The sensing volume refers to the physical space within which the spin defects can detect external perturbations, such as magnetic fields, temperature, or rotation. In the context of nanophotonic quantum sensing, the sensing volume is critical for applications requiring micro- to nanoscale spatial resolution. Resonant nanophotonic structures, such as cavities, metasurfaces, and slow-light waveguides, are designed to optimize the use of compact sensing volumes. These structures enhance spin-optic coupling and improve readout fidelity, enabling high sensitivity even in confined volumes. Photonics and micro-cavities enhance the absorption signal by concentrating electric field energy density, making them suitable for small sensing volumes. Plasmonic cavities and metasurfaces allow scalable sensing volumes while maintaining high sensitivity through sub-wavelength structures.

To significantly boost the CE in magnetometry applications, a chip-scale integrated SiC photonics platform presents a powerful solution. By fabricating waveguides and resonant structures directly within the SiCOI material, photons emitted by the V2 or PL6 centers can be efficiently coupled and routed on-chip. For instance, grating couplers can be optimized to extract light emitted in a specific direction, overcoming the limitations of total internal reflection in bulk SiC. Furthermore, integrating photonic crystal cavities or micro-ring resonators with the V2 centers can enhance the interaction between the emitted photons and the spin defects, leading to Purcell's enhancement of the emission rate and increased photon collection. This integrated approach not only minimizes losses due to free-space propagation and collection optics but also enables compact, scalable designs suitable for arrayed sensors and multiplexed readout, crucial for advanced magnetometry applications.

6.6. Micro and nanostructures

Engineering far-field radiation patterns for improved photon collection has been an area of significant effort using bulk optics combined with micron and sub-wavelength nanostructures on bulk diamond and SiC.

Hemispherical solid immersion lenses (SILs) depicted in figure 5(a), provide an enhancement of 3–4.4 for V_{Si} [106] and a factor of 5 for PL6 (single PL6 $>$ 550 kcounts s^{-1}); a factor of 9 enhancement including plasmonic effect within SIL, reaching up to $>$ 1 Mcounts s^{-1} for a single PL6 at saturation is demonstrated [107]. It has been shown that the ODMR contrast and spin coherence are generally preserved in the micro-nano-structures but the contrast is generally not always enhanced [107, 108]. SILs are favorable for emitters dipole in plane, as such not ideal for the V_{Si}.

Micropillars with sub submicron diameter [112] have shown a maximum fluorescence CE enhancement of a factor of 20 (7) for the ensemble of V_{Si} (NV in SiC, $N_C V_{Si}$), and a factor of 14 (8) for single $N_C V_{Si}$ in SiC nanopillars [109], as shown in figures 5(b) and (c). It has been demonstrated that micro pillars with submicron diameter can achieve a maximum CE of 40%–45% using individual pillars [113, 114], compared

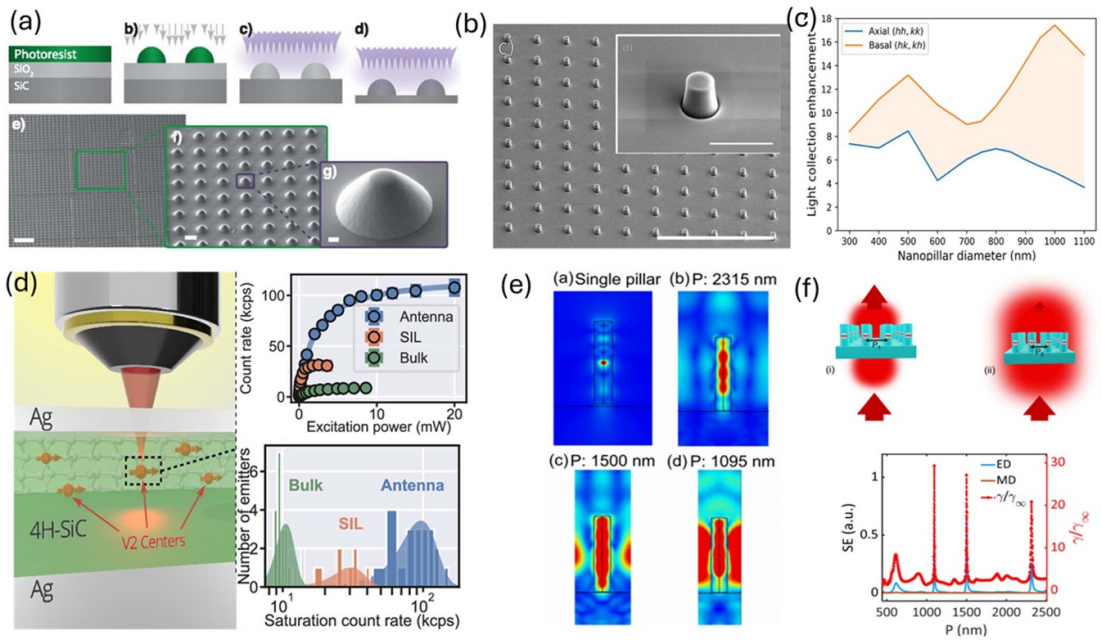

Figure 5. (a) SEM images showing scalable fabrication of SiC solid immersion lenses (SILs). (b) SEM images of an array of SiC nanopillars and a single pillar. (c) Simulated collection efficiency for a nitrogen-vacancy center in a SiC nanopillar, showing dependence on the emitter's dipole orientation. (d) Plasmonic planar antenna design for enhancing V2 center fluorescence, with a comparison of photon count rates from bulk SiC, a SIL, and the antenna. (e) Simulation of the electric field profile within a single SiC pillar and a lattice of pillars with varying periodicities. (f) Calculated decay rate of a V2 center in a SiC pillar lattice, showing enhancement due to Mie resonances. (a) Reproduced from [106]. CC BY 4.0. (b) and (c) Reprinted with permission from [109]. Copyright (2025) American Chemical Society. (d) Reprinted with permission from [110]. Copyright (2024) American Chemical Society. (e) and (f) © [2023] IEEE. Reprinted, with permission, from [111].

to ≈ 0.5% using the microscope objective only, if the localization of the emitters in the pillars is well controlled and the pillars size is designed. The CE, however depends on the emitter's dipole orientation and location in the material, as such nanopillars are more favorable for emitters dipole oriented vertically along the pillar's axis as shown experimentally by [109]. Generally, nanopillars contribute to a theoretical $F_p \approx 2.3$, which is rarely observed experimentally due to the need of exact positioning of the emitters dipole in the micropillars (approximately placed at $\lambda/2$ from the top or in the middle of the nanopillars) [113], as such other plasmonic resonators can be combined to reach theoretical $F_p \approx 7-8$ [104].

Other approaches rely on the use of 12.5 μm SiC membranes, combined with surface plasmon generated by gold film coplanar waveguides located at 15 nm from the PL6 emitters, with a factor of 7 enhancement of the fluorescent CE for single PL6 (>1 Mcounts s^{-1} at saturation for single PL6 with NA $= 1.4$) [115]. While the spin coherence is not degraded in the thin film, the co-planar waveguide increases the Rabi frequency up to 14 times due to improved MW power excitation/delivery.

Another simple approach is to use dielectric microcavities based on thin film SiC providing a 1.6-fold improvement in magnetic field sensitivity [116].

Using a planar cavity optical antenna based on a 135 nm-thin membrane of 4H-SiC silver-coated as shown in figure 5(d), a broadband resonance yields a mean (maximum) count rate enhancement factor of 9 (15) for single V2 with saturation count rate of 119 kcounts s^{-1} [110] (figure 5(d)). Planar optical antennas are providing the best enhancement if combined with microscope objectives, compared with nanopillars and SILs, which depends on the exact positioning of the emitters. Using a pillar lattice array instead of a single pillar (figure 5(d)), it is theoretically shown that a fluorescence enhancement of a theoretical factor of 30 could be achieved for the V2 line [111] due to Mie-superposition of the electric dipolar and magnetic quadrupolar electromagnetic Mie-scattering moments of the structure and it is less reliant on the dipole positioning and favorable for dipoles oriented in plane (figure 5(d)). All these approaches are however not always scalable or less integrable on chip.

6.7. Integrated waveguides

The collection of the emitted light by color centers in bulk and their coherent, resonant optical excitation is inefficient for several factors. A primary factor is that their dipolar emission pattern is generally a poor match to free space collecting optics, such as microscope objective or even nanopillars, thus the CE is limited to 40%–60%. This is especially true for the V2 line of silicon vacancy in 4H-SiC, whose dipole (TM polarized)

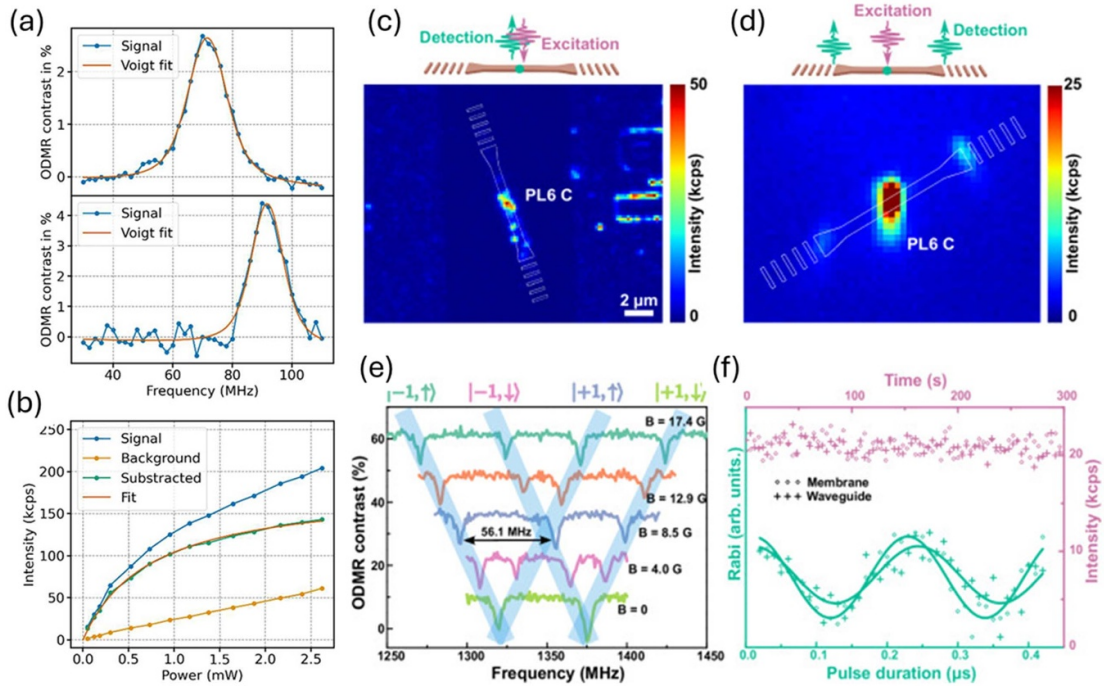

Figure 6. (a) ODMR spectrum of two V2 centers within a photonic waveguide. (b) Photon saturation curve for a single V2 center in the waveguide. (c) Confocal scan image of a PL6 center integrated into a waveguide. (d) Top-down collection map of PL6 fluorescence. (e) ODMR spectra of the waveguide-integrated PL6 center, showing hyperfine coupling to a ^{13}C nuclear spin at different magnetic fields. (f) Rabi oscillations of a PL6 spin in a membrane versus in a waveguide. (a) and (b) Reprinted with permission from [119]. Copyright (2024) American Chemical Society. (c)–(f) Reproduced from [120], with permission from Springer Nature.

emission is strongest in the plane, while the emission towards the vertical direction is the weakest. In addition, significant total internal reflection at the SiC-air interface is an additional detriment. In contrast, color centers embedded in engineered on-chip waveguides or cavities can directly emit into waveguided or spatially confined optical spatial modes with very high efficiency [117]. This will help improve the photon CE by orders of magnitude in the ODMR, which is a key factor limiting sensitivity. The photonics in-plane geometry allows seamless coupling of the emitters to the waveguides through evanescent fields, enabling low-loss on-chip photon routing and modular interconnects for scalable architectures. Efforts are ongoing to integrate the V2 line in photonics. Single V2 created by He ions implantation has a long spin coherence time of 1.4 ms, which is preserved in triangular cross section waveguides to 840 ns, with a high optical spectral stability of 29–40 MHz [66]. $T_2 = 9.4 \pm 0.7\,\mu$s of single V2 was determined in the waveguide, which is only twice shorter than deep-bulk defects in the same sample. Therefore, the spin dephasing of the V2 can be somehow preserved in the fabricated waveguides. These triangular cross-section waveguides can be directly applied to bulk substrates of any polytype [118]. It was shown that the coupling efficiency, CE, of the V2 centered in the waveguide into the fundamental TE waveguide is a function of the waveguide width and can be as high as 82% [119] and it is generally >40%. In this case the V2 center dipole is parallel to the top surface of the waveguides as the sample was grown along the *a* side with a slightly higher nitrogen concentration, and V2 was created using electron irradiation, as such the position of the emitter in the waveguide is not controlled. In a waveguide the $R \propto \mathrm{CE} \cdot \eta_{\mathrm{tr}} \cdot \eta_{\mathrm{out}} \cdot \mathrm{QE}$, which include the waveguide transmission losses (η_{tr}) and the out-coupling efficiency (η_{out}). While by designing the waveguide and positioning the V2, it is possible to achieve higher coupling efficiency, CE, it is also necessary to collect the photons out of the waveguide. Several approaches can be used to extract photons from waveguides such as grating couplers with outcoupling efficiencies of 83%, 3D tapered waveguide-to-fiber couplers and tapered fibers with $\eta_{\mathrm{out}} = 93\%$. The V2 emission integrated in the waveguide was collected by tapered fiber with 93% CE, where exhaustive simulations on the critical parameters of fiber/waveguide interface to reduce transmission losses, η_{tr}, were performed. In the waveguide it has been observed a photon count enhancement of 20-fold compared to V2 in bulk material (140 kcounts s^{-1} for single V2) and an ODMR contrast above 4% [119] (see figures 6(a) and (b)). The spin coherence of V2, $T_2 = (42.5 \pm 5.3)\,\mu$s in absence of any externally applied magnetic field, large compared to previously reported values for bulk emitters.

A modified divacancy PL6 was integrated into a waveguide in SiCOI, excited in the confocal configuration, while the emission was collected using grating couplers [120] (figures 6(c) and (d)). The

quantum emitter was integrated in the waveguide developing a nanoscale positioning technique via direct camera imaging and pattern recognition achieving a positioning accuracy of a single close to 10 nm. Within the waveguide an electron-nuclear quantum register based on PL6 was achieved as shown by the ODMR spectra and Rabi Oscillation in figures 6(e) and (f). The T_2^* of the PL6 in the waveguide was 0.94± 0.17 μs, comparable to the values before the integration in the membrane as the SiC wafer was a basic commercial sample [120].

It is therefore expected that with careful design of the waveguide and grating couplers in SiCOI with higher purity material, high CE and detection can be achieved to improve the photon detection rate R even without the use of Purcell's enhancement.

6.8. Resonant photonic cavity

With resonant nanophotonic structures one can modify the rate of radiative emission through density-of-states engineering, thus increasing F_p while simultaneously increasing the CE. The magnetic field sensitivity thus scales with $\sqrt{F_p \times CE}$. The Purcell's factor in a resonant cavity is determined by the specific nanophotonic structure, effective mode volume V_{eff} (order of $0.1(\lambda_0/n_{cavity})^3$, λ_0 free-space wavelength associated with the transition [121]), quality factor Q up to $10^6 - 10^7$ for photonic crystals and ring resonators, resonance wavelength λ_{cavity} and refractive index of the cavity at resonance n_{cavity}, such as [122]:

$$F_p = \frac{3}{4\,\pi^2} \times \frac{Q}{V_{eff}} \times \left(\frac{\lambda_{cavity}}{n_{cavity}}\right)^3 \times DW \times \frac{\left|\vec{E}\right|^2}{\left|\vec{E}_{max}\right|^2} \cos\phi + 1. \tag{9}$$

If the cavity is coupled with a quantum emitter, F_p is generally reduced by the spatial overlap and spectral matching between the emitter and the cavity mode, respectively, equal to one in the case of perfect coupling. DW factor quantifies the spectral overlap, $\left|\vec{E}_{max}\right|$ is the maximum electric field of the resonator mode, $\left|\vec{E}\right|$ is the electric field intensity at the color center, and Φ is the angle between the orientation of color center dipole and the electric field. $\frac{\left|\vec{E}\right|^2}{\left|\vec{E}_{max}\right|^2}$ accounts for the spatial overlap of the electromagnetic field in the cavity with the one of the color centers.

In the case of several color centers in the cavity the enhancement scales with the density of color centers in the cavity mode volume.

To achieve high Purcell's enhancement high Q and small V_{eff} are therefore preferred. V_{Si} has already been integrated in photonic chips based on SiCOI without deteriorating its quantum properties [64].

Two V2 emitters were coupled to a microdisk resonator with loaded cavity $Q = 1.3\times10^5$ integrated with a waveguide, obtaining a detection rate of 800 000 cts s^{-1} at saturation in the cavity corresponding to a 40-fold increase compared to bulk emitters [123] (figures 7(a) and (b)).

The local electric-field intensity inside a photonic cavity scales as $\propto \eta_c \frac{Q}{V_{eff}}$, where η_c is the input power-coupling efficiency with the cavity.

The photonic integration therefore allows more efficient excitation of the quantum emitter. In fact $R \propto \frac{\xi\, P_{opt}}{E_{ph}}$ [24], where ξ is the fraction of excitation photons converted to fluorescence photoelectrons, and E_{ph} is the excitation photon energy. The photonics improves the ξ factor, thus providing higher detected photons. Additionally, the excitation intensity is localized in a smaller material volume, thus interrogating fewer centerges and spins near the quantum emitter, thus reducing spin and spectral dephasing mechanism and improving the photoemission stability and the spin-coherence time.

6.9. Photonic microcavity

Photonic microcavities are structures that confine light to small volumes $(12\times\lambda^3)$ using highly reflective mirrors and moderate $Q \approx 10\,000$–$70\,000$, increasing the interaction time between light and matter within the cavity. Common examples include Fabry–Perot cavities, that offer easy tunability of the spatial and spectral position of the cavity resonance. Microcavities can boost the photon emission rate from V2 line, leading to improved signal-to-noise ratios and higher sensitivity. Hessenauer *et al* [124] demonstrated cavity enhancement of V_{Si} centers in 4 H-SiC using a fiber-based Fabry–Perot microcavity with $Q \approx 74\,000$. Compared with integrated structures, fiber-based Fabry–Perot cavities offer the possibility of easy tunability of the spatial and spectral position of the cavity resonance. Their work uses a tunable, fiber-based cavity to couple to the zero-phonon line of the V2 silicon vacancy. This setup allows for precise control of the cavity resonance and efficient coupling to the emitter, and they demonstrated the capability to reduce the photoluminescence lifetime with 13.3-fold Purcell enhancement of the ZPL of a single emitter, a key step for future improvement of SiC magnetometry. This approach demonstrates the potential of microcavities to

enhance the performance of SiC-based quantum sensors, paving the way for more sensitive and compact devices.

6.10. Plasmonic cavities

Plasmonic cavities leverage the interaction between light and free electrons in metals, typically gold or silver, to confine light to sub-wavelength dimensions. When light interacts with a metallic nanostructure, it excites collective oscillations of electrons known as surface plasmons. These plasmons can create extremely small and intense electromagnetic fields, concentrating light into volumes far smaller than the diffraction limit (as small as $10^{-6}(\lambda_0/n_{\text{cavity}})^3$), for optical fields confined in the gap between two closely spaced plasmonic resonators, opposite to photonic cavity, which are diffraction limited. This strong field enhancement makes plasmonic cavities ideal for boosting light-matter interactions, increasing the emission rate of nearby quantum emitters like silicon vacancies, and improving the sensitivity of quantum sensors in sub-diffraction volume. In fact, the spontaneous emission enhancement due to a plasmonic cavity mode is $F_{\text{p}} = \frac{3}{2\pi^2}\frac{W_{\text{E}}}{W_{\text{E}}+W_{\text{M}}}\frac{Q}{V_{\text{eff}}}(\frac{\lambda_{\text{cavity}}}{n_{\text{cavity}}})^3$, where W_{E} and W_{M} are the stored electric and magnetic energies, respectively [125], a similar expression of a photonic cavity, except that $Q \lessapprox 100-1000$ is generally small due to metallic losses, permitting a broad emission enhancement, while V_{eff} can scale with the plasmonic cavity dimensions. In addition, nanoantennas can shape the far-field emission of the optical emitter dipole and create a directional pattern that maximizes power within a given NA [126]. The trade-off is that plasmonic cavities often have high losses due to the inherent absorption in metals, which can limit their overall efficiency, and have a low Q. Due to highly localized plasmonic modes, spin defects must be in nanometric proximity to the plasmonic structure for emission enhancement to be significant, which is challenging with the use of bulk diamond or SiC, where the placement of defects close to the surface (within 100 nm) significantly reduce their spin coherence. However recently integrating the V_{Si} in a silver SiC plasmonic nanocavity with $Q \approx 800$ and mode volume $0.45(\frac{\lambda_{\text{cavity}}}{n_{\text{cavity}}})^3$, an experimental $F_{\text{p}} = 48$ was achieved to excite in resonance spin selective transition of the V_{Si} V1 lines (figures 7(c) and (d))[127].

6.11. On-chip on resonance photonic cavity

On-chip photonic structures allow as well resonant excitation of color centers with spatial separation of the resonant pump. In resonant excitation, a 3 C-SiC photonic crystal cavities with a modest $Q = 1550$ with integrated divacancies provided a factor of 30 increase in the PL and ODMR contrast and a 705-fold reduction in excitation mode volume compared to bulk material, overcoming the spectral inhomogeneous broadening of the emitter [129]. The ODMR enhancement under resonant excitation is due to higher PL count rates and due to an increase of the rate of optically induced spin polarization in divacancy GS as a result of the excitation enhancement provided by the resonant cavity mode. These small mode volumes and excitation intensity enhancements can greatly improve quantum sensing based on on-chip defects, rather than using a bulk material waveguide that traps light [130]. Purcell's enhancement of $F_{\text{p}} = 50$ was measured for divacancy in the photonic crystal cavity, providing a higher Rabi oscillation contrast and extended spin coherence [122]. The coupling of PL4 divacancy with tunable microring resonators with $Q = 1261$ in thin-film 4 H-SiCOI nanophotonics provided a Purcell factor enhancement of $F_{\text{p}} = 5$, which confined coherent photons within the coupled waveguide, resulting in a 2-fold increase in the ODMR contrast [128] compared to collection from the confocal objective, as shown in figures 7(e)–(j). On-chip waveguide and resonators can selectively couple different emission branches of the modified divacancy based on emission polarization and mode matching with the waveguide and thus improve the spin-read out fidelity compared to out of plane collection [79]. On-chip SiC-based electro-optic modulator can enable cavity tuning, pulsed pumping and implementation of Ramsey interferometry in ODMR [131, 132]. The design and fabrication of an optimized 4 H-SiC electro-optic modulator at 920 nm in the V2 line emission with a propagation loss of less than 0.3 dB cm^{-1} was demonstrated in a SiCOI waveguide coupled with micro-ring resonators [132]. As such, we anticipate significant improvements in the excitation efficiency and ODMR contrast, which will translate into improvements in magnetic field sensitivity in on-chip magnetometry.

6.12. Metasurfaces

Metasurfaces are artificially engineered structures decorated by sub-wavelength resonators designed to provide collective electromagnetic properties not available in bulk materials. These properties arise from the collective response of close nanoresonators, rather than the intrinsic properties of the constituent material. For quantum sensing, metamaterials can be used to create highly efficient light-trapping structures or to manipulate the emission properties of color centers, enhancing both excitation and CE. A metasurface is designed to scatter light impinging from the far-field and act as nanoantenna coupling the light emitter in the near field to the far-field with the desired properties. The quantum emitter should be localized in the near field of the nanoantennas. The metasurfaces are also driven by the near field quantum emission in

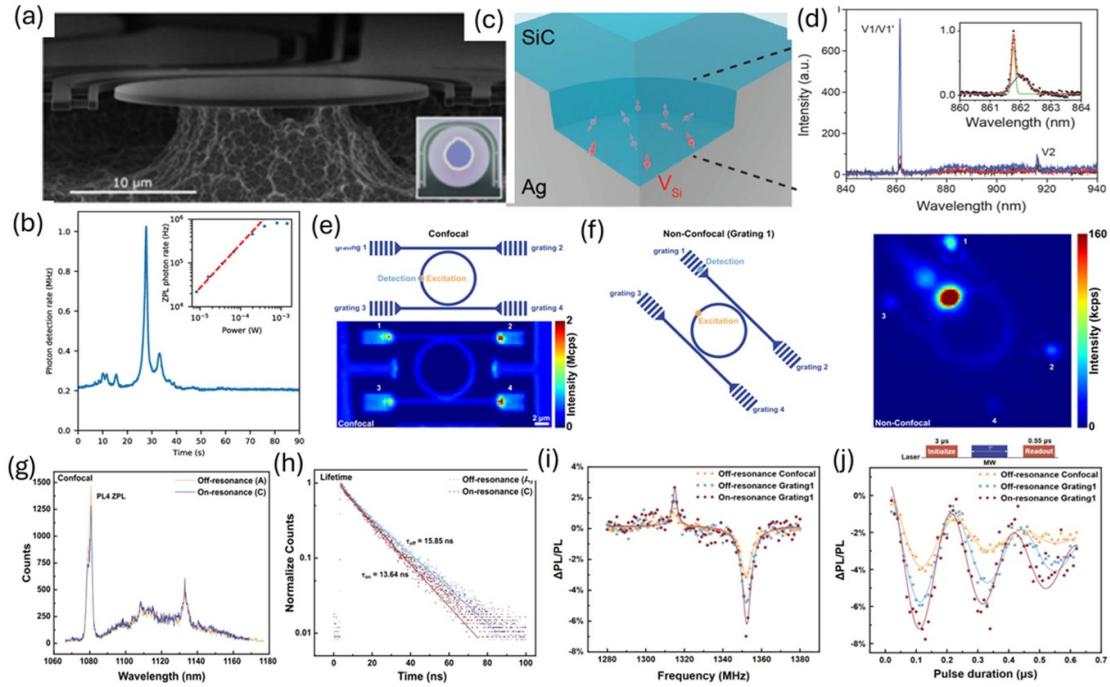

Figure 7. (a) SEM of a microdisk resonator coupled to a waveguide. (b) Photon detection rate demonstrating Purcell enhancement for the V2 zero-phonon line (ZPL). (c) Design of a plasmonic cavity integrated with V1 and V1' V_{Si} centers. (d) PL spectra of V_{Si} centers showing a 48-fold Purcell enhancement with resonant excitation. (e) Confocal map of a microring cavity with grating couplers. (f) Emission collected from four distinct grating couplers, showing PL4 center light routed through the waveguide. (g) PL spectra showing emission enhancement when the cavity is tuned on-resonance with the PL4 ZPL. (h) Lifetime measurements showing a Purcell factor of 5 for the cavity-coupled PL4. (i) ODMR spectra showing a 2-fold contrast enhancement when collected through the resonant microring. (j) Rabi oscillations showing enhanced contrast for the cavity-coupled PL4 spin. (a) and (b) Reproduced from [123]. CC BY 4.0. (c) and (d) Reprinted with permission from [127]. Copyright (2024) American Chemical Society. (e)–(j) Reprinted with permission from [128]. Copyright (2025) American Chemical Society.

addition to the incident far field light. A quantum metasurface therefore is broadly defined as a two-dimensional arrangement of nanoantennas driven by localized quantum sources located in the near field, providing emission enhancement via the Purcell's effect, and engineered to provide spectral and directional shaping of the emitted light [133]. Purcell's enhancement of quantum emitters in metasurfaces is typically achieved using various resonance phenomena such as plasmonic, Mie-resonance, bound states in the continuum (BIC) [134], lattice resonances. These metasurfaces exhibit sharp Fano resonances in the their reflection and transmission properties at specific wavelength as per design, that modifies the local density of state resulting in photoluminescence enhancement and far-field emission directionality of an integrated dipole. Example of metasurfaces are hyperbolic metamaterials (HMM), a highly dispersive metal-dielectric nanoscale hybrid structures, made of alternating ultrathin films of metals and dielectric materials. HMM create an effective highly anisotropic material with hyperbolic dispersion, supporting optical modes with ultrahigh K-vectors, thus useful to control the emission of atomic dipoles. Their employment in conjunction with NV in nanodiamonds has shown ODMR with narrower resonances and better signal to noise ratio [135]. For perpendicular dipole orientation relative to the interface, the HMM-coupled antenna resonator could lead to a large spontaneous emission enhancement with a Purcell's factor of the order of 250, along with a very high average total overall collected photon rate of about 80 at 900 nm close to the V_{Si} emission as previouslu modeled [136]. Optically addressable spin defects ensemble of negatively centerged boron vacancy defects in hBN were coupled to BIC metasurface, resulting in a 25-fold increase in photoluminescence intensity and spectral linewidth below 4 nm of the coupled emitters [137]. The ODMR of the spin defects was demonstrated in the metasurface with increased spin read-out efficiency, however the current experiments are not providing clear advances in quantum sensing applications.

7. Magnetometry based on V2 and PL6 in SiC

In this section we will first review the current state of the art of SiC quantum magnetometers based on V2 and PL6 lines, compare them with the NV in diamond and then we will discuss foreseeable improvements based on integrated photonics.

7.1. Current performance of SiC magnetometers

For practical applications such as brain-wave sensing, achieving a sensitivity on the order of fT/$\sqrt{\text{Hz}}$ within a small volume is critically important. For V2 magnetometry, a preliminary experiment has demonstrated room-temperature sensitivity of 50 nT/$\sqrt{\text{Hz}}$ [18]. In this experiment conditions [18], the shot-noise-limited sensitivity was 3.5 $\frac{fT}{\sqrt{\text{Hz}}}$. The V_{Si} was created by neutron irradiation and subsequent annealing at 600 °C for 4 h, then thermally quenched by quickly removing them from the furnace at the end of the anneal and immersing them in a water bath. Thermal quenching reduces the formation of carbon-antisite defects or other defects from the V_{Si} during the time the samples returns to room temperature. A concentration of $10^{15} V_{Si}$ cm^3 is estimated. This annealing improves up to $C_{CW-ODMR} \approx 1.8\%$, with the optical power of 400 mW and RF power of 1 W, the $\Delta\nu < 7$ MHz ($T_2^* \approx 1/\pi\,\Delta\nu = 44$ ns) and the brightness $R \approx 2 \times 10^{13}$ counts s^{-1} ($\approx$3 μW photoluminescence detected). The short T_2^* is here possibly due to the neutron irradiation producing high defects density and the starting material being a high-purity semi-insulating SiC substrate. Using isotopically purified 4 H-SiC epilayers (^{13}C = 0.15% and ^{29}Si = 0.01%, natural isotopic abundance is ^{29}Si = 4.7%, ^{13}C = 1.1%), irradiated with electrons at 1 MeV with doses from 10^{17} to 10^{20} cm^{-2}, followed by thermal annealing at 700 °C, reference [91] has improved the V2 $T_2^* = 5.7$ μs for optimal dose of 10^{17} cm^{-2} (2.2 μs at doses of 10^{20} cm^{-2}). This would result in a shot-noise-limited sensitivity of $\approx$ 27 pT/$\sqrt{\text{Hz}}$, if the same contrast and count rate could be achieved in the same material. However, the contrast was only 0.06% thus the shot-noise-limited sensitivity could be improved to $\lessapprox 1$ nT/$\sqrt{\text{Hz}}$. Further improvement was achieved of $T_2^* > 20$ μs for the transition $(-1/2, 1/2)$ due to further suppression of strain induced dephasing for the specific transition, in this case with a contrast of 0.06% and a shot-noise-limited sensitivity of $\approx$ 200 pT/$\sqrt{\text{Hz}}$. For V2 the current shot-noise sensitivity based on bulk optics is estimated at 2 nT/$\sqrt{\text{Hz}}$ [8]. The highest measured sensitivity reached using the V2 line in bulk 4 H-SiC epilayers of 20 μm-thick has been 4 nT/$\sqrt{\text{Hz}}$ [8] limited by the magnetic field noise and laser-amplitude noise, thus better magnetic isolation and laser-amplitude noise reduction should lead to greater improvement using the Ramsey scheme. Here isotopically purified 4 H-SiC epilayers [91] with $T_2^* =$ 5.7 μs, were used and the ensemble of V_{Si} was created by irradiating the material with the highest doses of the electron beam of 3×10^{19} e-/cm^{-2}, followed by annealing in air at 700°C for 2 h. The excitation laser illuminates the V_{Si} along the emission direction for optical absorption and collection, which is perpendicular to the 4 H-SiC c-axis. The V_{Si} is detected by a lock-in amplifier and the spin control is achieved using CW ODMR and Ramsey sequence.

The use of single V2 in non optimized and commercial bulk SiC for quantum sensing has been just demonstrated [138], realizing 0.33 Hz high-resolution nanoscale nuclear magnetic resonance (NMR) with sensitivity of 358 μT/$\sqrt{\text{Hz}}$, more than two times larger than the theoretical value due to experimental imperfections and low ODMR contrast. Nevertheless, this resolution signals opportunity to measure chemical structure's molecular dynamics at the single-molecule level. Combining these sensors with integrated photonics an improved sensitivity can be achieved and can enable spatially separated sensors in parallel for large scale NMR Other examples of magnetometry using V_{Si} or other coler centers in SiC based on other approaches such as all-optical or all electrically detected spin read-out were recently reviewed by [6, 10] and can currently provide sensitivities in the range of 30–100 nT/$\sqrt{\text{Hz}}$.

For PL6 the ODMR contrast is around 23%, for PL5 18%, and for PL7 7%. The spin coherence time T_2 were in the range of 18–25 μs and $T_2^* < 1\mu$s using C-ions implantation [82], while using focused He-beam the spin-echo coherence T_2 was recently extended to 194 μs [79] with 160 gauss magnetic field and $T_2^* = 3\mu$s.

We here note that PL6 has been used for magnetometry with a sensitivity of 4 $\mu T/\sqrt{\text{Hz}}$ [102], currently limited by the low concentration of ensemble due to the current fabrication approaches and the generally shorter coherence time compared to the V_{Si}. Due to being robust at high temperature, the PL6 are nevertheless successfully used to study ferromagnetism in 2D materials [139]. Single PL6 for magnetometry has not yet been investigated and could yield opportunities in integrated photonics.

7.2. Comparison with diamond NV centers

The diamond NV's highest pulsed magnetometry sensitivity of 0.9 pT/$\sqrt{\text{Hz}}$ was achieved by applying a magnetic flux concentrator to enhance the local magnetic field by more than a factor of 200 (from 300 pT/$\sqrt{\text{Hz}}$), using 200 mW of optical power and 20 mW of MW power [140], while in the DC sensitivity for diamond NV of 2.6–6 pT/$\sqrt{\text{Hz}}$ was achieved with a diamond volume of (0.5 mm)^3 with NV center ensembles with an ODMR linewidth of $\Delta\nu = 28$ kHz and $T_2^* = 8.5$ μs and a factor of 2.67 contrast enhancement using 100 mW optical power [24]. In addition to the use of MW cavities, other strategies for enhancing NV magnetometry are based on the light-trapping diamond waveguide based on the total internal reflection of the input laser in the diamond slab that allows for increased pump laser absorption and photon collection, with possible improvement of $R \approx 10^{15}$ counts s^{-1}($\approx$300 μW photoluminescence detected), achieving a magnetic sensitivity of 290 pT/$\sqrt{\text{Hz}}$ [130]. This approach eliminates the need for excitation from

Table 1. Summary of the shot noise theoretical and measured DC sensitivity (CW ODMR) for V2 and PL6 in 4 H-SiC, NV in diamond.

Material	T_2^* (μs)	FWHM (MHz)	C (%)	R (counts/s)	Shot noise Sensitivity (nT/$\sqrt{\text{Hz}}$)	Measured Sensitivity (nT/$\sqrt{\text{Hz}}$)	References
4 H-SiC V2	0.044	7	1.8	2×10^{13}	3.5	50	[18]
4 H-SiC V2	5.7 (7.5)	0.06	0.06	3×10^{12}	2 (0.2 with Ramsey)	4	[8]
4 H-SiC PL6	0.5	11.9	1.8	1.0×10^{7}	500	4000	[102]
Diamond NV	8.5	0.03	10.7	1×10^{13}	0.003	0.0026–0.006	[24]

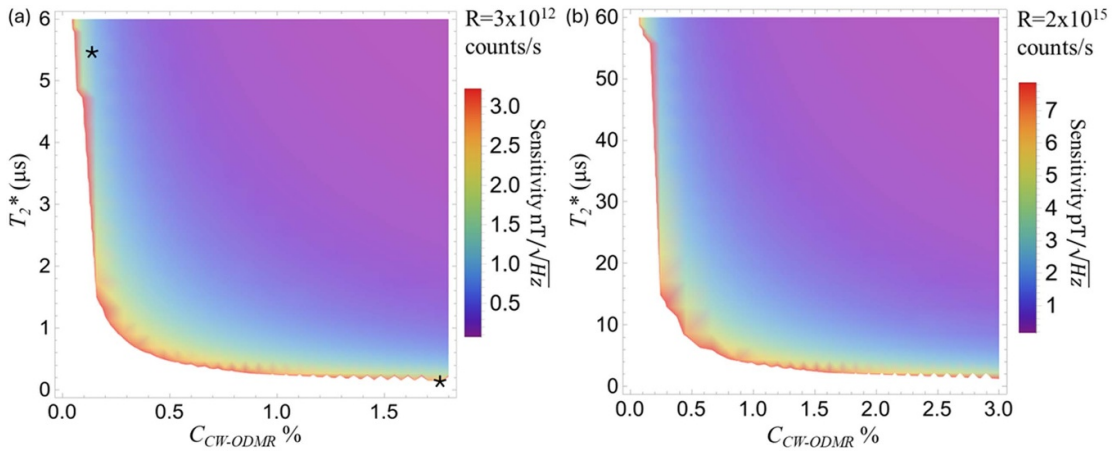

Figure 8. (a) Projected shot-noise-limited sensitivity for V2 centers in 4H-SiC, based on current bulk optics performance combined with material improvements to T_2^* and ODMR contrast, $C_{\text{CW}-\text{ODMR}}$. Stars indicate experimentally achieved sensitivities from references [8, 18]. (b) Projected sensitivity for V2 centers in 4 H-SiC assuming integration with a photonic cavity. The projection includes improvements in ODMR contrast ($C_{\text{CW}-\text{ODMR}}$) and photon detection rate (R) due to the cavity, alongside expected enhancements in spin coherence time (T_2^*) [66].

the top of the sample. Similar studies using enhanced absorption of the optical [130] and MW power [24], which can improve the ODMR contrast, have not yet been performed in V2 in 4 H-SiC, but it is expected that optimizing the optical and MW power [14] an order of magnitude improvement of the SiC sensitivity should be achieved in the bulk material.

In the case of SiC, all the above strategies can in fact be implemented to achieve higher sensitivity, however, these approaches are still bulky and less suitable for many applications of magnetic sensing. While using SiCOI waveguides with integrated V2 spin defects [120] could yield a relevant photon excitation and CE enhancement. In table 1 the experimental parameters to achieve the sensitivity for the above magnetometry demonstrations are listed, showing as one of the main limitations for bulk-SiC V2 to improve sensitivity is the low ODMR contrast compared to NV in diamond, while for bulk-SiC PL6 is the low ensemble of the defects that can be generated.

7.3. Projected sensitivity with integrated photonics

With further material and defects fabrication optimization also based on isotopic purification, in the case of V2, it could be possible to increase $T_2^* = 10$ μs level [141] using electrons irradiation and achieve shot-noise limited sensitivity of 15 pT/$\sqrt{\text{Hz}}$.

Improving the optical excitation using a photonic cavity, $C_{\text{CW}-\text{ODMR}}$ can be improved by a factor up to 10. The photonic waveguide cavity can improve the photon CE to at least CE = 80% and achieve the current demonstrated Purcell enhancement of 50 in the moderate $Q = 1000$–5500 cavity, for an overall factor of 30 increase in $R = 6 \times 10^{14}$ counts s^{-1} [122, 129], thus with the state of the art 4 H-SiCOI photonic resonators with $Q \approx 10^6$ [142], an additional factor of 10 improvement could be expected for R, thus $R \gtrsim 10^{15}(10^9)$ counts/s can be an achievable target for V2 (PL6).

When all the above strategies are combined, the shot-noise-limited sensitivity for V2 can be improved to $\lessapprox$ pT/$\sqrt{\text{Hz}}$ ($T_2^* = 15$ μs, $C = 3\%$, $R = 10^{15}$ photons/s) (see figure 8(b)). For PL6 using integrated photonics to improve the $C_{\text{CW}-\text{ODMR}}$ of a factor of at least 2 and R of a factor of 5 [128], combined with the current $T_2^* = 3$ μs [79], the sensitivity could be of $\lessapprox$12 nT/$\sqrt{\text{Hz}}$ ($T_2^* = 3$ μs, $C_{\text{CW}-\text{ODMR}} = 5\%$, $R = 5 \times 10^7$

photons/s)). Spin dephasing of $T_2^* = 70$–160 μs and 375 μs were achieved in natural abundance and isotopically purified divacancy in 4 H-SiC, respectively [90].

8. Conclusions

In this paper, we have presented the advantages of using integrated photonic waveguides and resonant cavities for improving the magnetic sensitivity of SiC-based optical spin qubits. Leveraging state-of-the-art SiCOI photonics, combined with ongoing improvements in spin defect fabrication and material optimization, offers a clear path toward next-generation quantum sensors. The integration of quantum defects like the V_{Si} and modified divacancy with photonic structures represents a crucial step toward practical devices that combine high sensitivity with scalable fabrication. With continued improvement of SiCOI photonic resonators toward higher Q-factors, on-chip quantum sensing can achieve a clear advantage over bulk-material demonstrations. In this view, sensitivities approaching the $\mathrm{pT}/\sqrt{\mathrm{Hz}}$ level are achievable within a small sensing volume, even in the weak coupling regime, providing a scalable and industrially compatible solution for quantum sensing applications. This performance level would enable detection of weak biomagnetic signals and nanoscale magnetic phenomena previously inaccessible to conventional sensors.

However, several challenges and trade-offs must be addressed. Enhancing radiative transitions via photonic structures can sometimes reduce spin contrast at room temperature, particularly for off-resonant excitation schemes [16]. This trade-off requires careful engineering of the photonic environment to balance brightness enhancement with the preservation of high spin-readout fidelity. Furthermore, while emerging platforms like quantum plasmonics and metasurfaces offer unique advantages in extreme field confinement, their practical benefit for quantum sensing is still under investigation. The fundamental physical limits of emission enhancement also warrant consideration; while plasmonic nanocavities can theoretically offer much higher photon rates than dielectric cavities, they suffer from higher losses [143]. Future research should therefore explore hybrid photonic-plasmonic resonators and other innovative designs that combine the best aspects of different platforms to push the performance of integrated quantum sensors while maintaining practical operating conditions.

Data availability statement

No new data were created or analysed in this study.

Funding statement

No funding was received for this work.

Conflict of interest

The authors have no competing interests.

Generative AI and AI-Assisted Technologies

Generative AI and AI-assisted technologies were not used.

Author contributions

S Castelletto 0000-0002-8675-2291
Conceptualization (lead), Methodology (lead), Visualization (lead), Writing – original draft (lead), Writing – review & editing (lead)

A Boretti 0000-0002-3374-0238
Conceptualization (equal), Writing – original draft (equal), Writing – review & editing (equal)

References

[1] Degen C L, Reinhard F and Cappellaro P 2017 *Rev. Mod. Phys.* **89** 035002
[2] Schirhagl R, Chang K, Loretz M and Degen C L 2014 *Annu. Rev. Phys. Chem.* **65** 83–105
[3] Wolfowicz G, Heremans F J, Anderson C P, Kanai S, Seo H, Gali A, Galli G and Awschalom D D 2021 *Nat. Rev. Mater.* **6** 906–25
[4] Falk A L, Buckley B B, Calusine G, Koehl W F, Dobrovitski V V, Politi A, Zorman C A, Feng P X L and Awschalom D D 2013 *Nat. Commun.* **4** 1819

[5] Castelletto S, Johnson B and Boretti A 2013 *Adv. Opt. Mater.* **1** 609–25
[6] Castelletto S, Lew C T-K, Lin W-X and Xu J-S 2023 *Rep. Prog. Phys.* **87** 014501
[7] Castelletto S and Boretti A 2020 *J. Phys. Photon.* **2** 022001
[8] Lekavicius I, Carter S, Pennachio D, White S, Hajzus J, Purdy A, Gaskill D, Yeats A and Myers-Ward R 2023 *Phys. Rev. Appl.* **19** 044086
[9] Tahara K, Tamura S, Toyama H, Nakane J, Kutsuki K, Yamazaki Y and Ohshima T 2025 *npj Quantum Inf.* **11** 58
[10] Luo Q Y *et al* 2023 *Front. Phys.* **11** 2023
[11] Castelletto S, Peruzzo A, Bonato C, Johnson B C, Radulaski M, Ou H, Kaiser F and Wrachtrup J 2022 *ACS Photon.* **9** 1434–57
[12] Kumela A, Gemta A, Hordofa A, Dagnaw H, Sheferedin U and Tadesse M 2023 *AIP Adv.* **13** 075301
[13] Lukin D M, Guidry M A and Vučković J 2020 *PRX Quantum* **1** 020102
[14] Barry J F, Schloss J M, Bauch E, Turner M J, Hart C A, Pham L M and Walsworth R L 2020 *Rev. Mod. Phys.* **92** 015004
[15] Aslam N, Zhou H, Urbach E K, Turner M J, Walsworth R L, Lukin M D and Park H 2023 *Nat. Rev. Phys.* **5** 157–69
[16] Kim L, Choi H, Trusheim M E, Wang H and Englund D R 2023 *Nanophotonics* **12** 441–9
[17] Zhang C *et al* 2023 *Front. Neurosci.* **16** 2022
[18] Abraham J B S *et al* 2021 *Phys. Rev. Appl.* **15** 064022
[19] Sánchez E D C, Pessoa A R, Amaral A M and Menezes L D S 2020 *AIP Adv.* **10** 025323
[20] Grinolds M S, Hong S, Maletinsky P, Luan L, Lukin M D, Walsworth R L and Yacoby A 2013 *Nat. Phys.* **9** 215–9
[21] Casola F, Van Der Sar T and Yacoby A 2018 *Nat. Rev. Mater.* **3** 1–13
[22] Katsumi R, Takada K, Kawai K, Sato D and Yatsui T 2025 *Commun. Mater.* **6** 1–8
[23] Quan W K, Liu L, Qin-Yue L, Liu X D and Wang J F 2023 *Opt. Express* **31** 15592–8
[24] Zhang C *et al* 2021 *Phys. Rev. Appl.* **15** 064075
[25] Stürner F M *et al* 2021 *Adv. Quantum Technol.* **4** 2000111
[26] Huang K, Mao X, Zhang Y, Wang M, He X, Ran G, Hu Q and Lin Z 2024 *IEEE Trans. Instrum. Meas.* **73** 1–9
[27] Ibrahim M I, Foy C, Englund D R and Han R 2021 *IEEE J. Solid-State Circ.* **56** 1001–14
[28] Chatzidrosos G, Wickenbrock A, Bougas L, Leefer N, Wu T, Jensen K, Dumeige Y and Budker D 2017 *Phys. Rev. Appl.* **8** 044019
[29] Eisenach E R, Barry J F, O'Keeffe M F, Schloss J M, Steinecker M H, Englund D R and Braje D A 2021 *Nat. Commun.* **12** 1–7
[30] Kominis I K, Kornack T W, Allred J C and Romalis M V 2003 *Nature* **422** 596–9
[31] Budker D and Romalis M 2007 *Nat. Phys.* **3** 227–34
[32] Shah V K and Wakai R T 2013 *Phys. Med. Biol.* **58** 8153
[33] Esmaeili S *et al* 2024 *APL Mater.* **12** 040901
[34] Kim D, Ibrahim M I, Foy C, Trusheim M E, Han R and Englund D R 2019 *Nat. Electron.* **2** 284–9
[35] Schall F, Hahl F A, Lindner L, Vidal X, Luo T, Zaitsev A M, Ohshima T, Jeske J and Quay R 2025 *Opt. Express* **33** 10899–910
[36] Wang J, Sciarrino F, Laing A and Thompson M G 2020 *Nat. Photon.* **14** 273–84
[37] Aghaee R H *et al* 2025 *Nature* **638** 1–8
[38] Lipton J *et al* 2025 *ACS Photon.* **12** 2397–405
[39] Sörman E, Son N T, Chen W M, Kordina O, Hallin C and Janzén E 2000 *Phys. Rev. B* **61** 2613–20
[40] Simin D, Kraus H, Sperlich A, Ohshima T, Astakhov G V and Dyakonov V 2017 *Phys. Rev. B* **95** 161201
[41] Ivády V, Davidsson J, Tien Son N, Ohshima T, Abrikosov I and Gali A 2017 *Phys. Rev. B* **96** 161114(R)
[42] Shang Z, Hashemi A, Berencén Y, Komsa H P, Erhart P, Zhou S, Helm M, Krasheninnikov A V and Astakhov G V 2020 *Phys. Rev. B* **101** 144109
[43] Kraus H, Soltamov V A, Fuchs F, Simin D, Sperlich A, Baranov P G, Astakhov G V and Dyakonov V 2014 *Sci. Rep.* **4** 5303
[44] Fuchs F, Stender B, Trupke M, Simin D, Pflaum J, Dyakonov V and Astakhov G V 2015 *Nat. Commun.* **6** 1–7
[45] Widmann M *et al* 2015 *Nat. Mater.* **14** 164–8
[46] Carter S G, Soykal O O, Dev P, Economou S E and Glaser E R 2015 *Phys. Rev. B* **92** 161202(R)
[47] Soltamov V A *et al* 2015 *Phys. Rev. Lett.* **115** 247602
[48] Economou S E and Dev P 2016 *Nanotechnology* **27** 504001
[49] Soykal O O, Dev P and Economou S E 2016 *Phys. Rev. B* **93** 081207
[50] Anisimov A N, Simin D, Soltamov V A, Lebedev S P, Baranov P G, Astakhov G V and Dyakonov V 2016 *Sci. Rep.* **6** 33301
[51] Bracher D O, Zhang X and Hu E L 2017 *Proc. Natl Acad. Sci.* **114** 4060–5
[52] Nagy R *et al* 2018 *Phys. Rev. Appl.* **9** 034022
[53] Fischer M, Sperlich A, Kraus H, Ohshima T, Astakhov G V and Dyakonov V 2018 *Phys. Rev. Appl.* **9** 54006
[54] Tarasenko S A, Poshakinskiy A V, Simin D, Soltamov V A, Mokhov E N, Baranov P G, Dyakonov V and Astakhov G V 2018 *Phys. Status Solidi b* **255** 1–9
[55] Davidsson J, Ivády V, Armiento R, Ohshima T, Son N T, Gali A and Abrikosov I A 2019 *Appl. Phys. Lett.* **114** 2–7
[56] Banks H B, Soykal O O, Myers-Ward R L, Gaskill D K, Reinecke T L and Carter S G 2019 *Phys. Rev. Appl.* **11** 1
[57] Udvarhelyi P, Nagy R, Kaiser F, Lee S Y, Wrachtrup J and Gali A 2019 *Phys. Rev. Appl.* **11** 1
[58] Dong W, Doherty M W and Economou S E 2019 *Phys. Rev. B* **99** 184102
[59] Bathen M E, Galeckas A, Müting J, Ayedh H M, Grossner U, Coutinho J, Frodason Y K and Vines L 2019 *npj Quantum Inf.* **5** 111
[60] Nagy R *et al* 2019 *Nat. Commun.* **10** 1954
[61] Singh H, Anisimov A N, Nagalyuk S S, Mokhov E N, Baranov P G and Suter D 2020 *Phys. Rev. B* **101** 134110
[62] Udvarhelyi P *et al* 2020 *Phys. Rev. Appl.* **13** 1–10
[63] Morioka N *et al* 2020 *Nat. Commun.* **11** 1–8
[64] Lukin D M *et al* 2020 *Nat. Photon.* **14** 330–4
[65] Nagy R *et al* 2021 *Appl. Phys. Lett.* **118** 144003
[66] Babin C *et al* 2022 *Nat. Mater.* **21** 67–73
[67] Morioka N *et al* 2022 *Phys. Rev. Appl.* **17** 054005
[68] Koehl W F, Buckley B B, Heremans F J, Calusine G and Awschalom D D 2011 *Nature* **479** 84–87
[69] Christle D J, Falk A L, Andrich P, Klimov P V, Hassan J U, Son N T, Janzén E, Ohshima T and Awschalom D D 2015 *Nat. Mater.* **14** 160–3
[70] Klimov P V, Falk A L, Christle D J, Dobrovitski V V and Awschalom D D 2015 *Sci. Adv.* **1** e1501015
[71] Zwier O V, O'Shea D, Onur A R and van der Wal C H 2015 *Sci. Rep.* **5** 10931
[72] Zhou J Y *et al* 2021 *ACS Photon.* **8** 2384–91

[73] Anderson C P *et al* 2022 *Sci. Adv.* **8** eabm5912
[74] Wolfowicz G, Anderson C P, Yeats A L, Whiteley S J, Niklas J, Poluektov O G, Heremans F J and Awschalom D D 2017 *Nat. Commun.* **8** 1876
[75] Zeledon C *et al* 2025 Minute-long quantum coherence enabled by electrical depletion of magnetic noise (arXiv:2504.13164)
[76] Anderson C and Awschalom D 2023 *Phys. Today* **76** 27–33
[77] Miao K C *et al* 2019 *Sci. Adv.* **5** eaay0527
[78] Mu Z *et al* 2020 *Nano Lett.* **20** 6142–7
[79] He Z X *et al* 2024 *Nat. Commun.* **15** 10146
[80] Son N T, Shafizadeh D, Ohshima T and Ivanov I G 2022 *J. Appl. Phys.* **132** 025703
[81] Golter D A and Lai C W 2017 *Sci. Rep.* **7** 13406
[82] Li Q *et al* 2022 *Natl Sci. Rev.* **9** nwab122
[83] Yan F F, Wang J F, Li Q, Cheng Z D, Cui J M, Liu W Z, Xu J S, Li C F and Guo G C 2018 *Phys. Rev. Appl.* **10** 044042
[84] Yan F F *et al* 2020 *Npj Quantum Inf.* **6** 1–6
[85] Chen Y *et al* 2025 Atomic structure analysis of pl5 in silicon carbide with single-spin spectroscopy (arXiv:2504.07558)
[86] Hao Z H, He Z X, Maksimovic J, Katkus T, Xu J S, Juodkazis S, Li C F, Guo G C and Castelletto S 2025 *ACS Photon.* **12** 1552–60
[87] Ivády V *et al* 2019 *Nat. Commun.* **10** 1–8
[88] Bulancea-Lindvall O, Son N T, Abrikosov I A and Ivády V 2021 *npj Comput. Mater.* **7** 1–11
[89] Kraus H, Soltamov V A, Riedel D, Väth S, Fuchs F, Sperlich A, Baranov P G, Dyakonov V and Astakhov G V 2014 *Nat. Phys.* **10** 157–62
[90] Bourassa A *et al* 2020 *Nat. Mater.* **19** 1319–25
[91] Lekavicius I *et al* 2022 *PRX Quantum* **3** 010343
[92] Chiba Y, Yamazaki Y, Sato S I, Makino T, Yamada N, Satoh T, Hijikata Y and Ohshima T 2020 Enhancement of odmr contrasts of silicon vacancy in sic by thermal treatment *Silicon Carbide and Related Materials 2019* (*Materials Science Forum*) vol 1004 (Trans Tech Publications Ltd) pp 337–42
[93] Wang X, Zhao M, Bu H, Zhang H, He X and Wang A 2013 *J. Appl. Phys.* **114** 194305
[94] Chen Y-C *et al* 2019 *Nano Lett.* **19** 2377–83
[95] Wang J, Song Y, Dong B, Zhao Y, Sun Q, Yan M, Yao C, Du Q and Xu Z 2024 *Ceram. Int.* **50** 46566–78
[96] Kasper C *et al* 2020 *Phys. Rev. Appl.* **13** 044054
[97] Wang J F *et al* 2019 *ACS Photon.* **6** 1736–43
[98] He Z X *et al* 2023 *ACS Photon.* **10** 2234–40
[99] Dong B, Sun Q, Wang J, Song Y, Ren F and Xu Z 2025 *Opt. Laser Technol.* **186** 112661
[100] Day A M, Dietz J R, Sutula M, Yeh M and Hu E L 2023 *Nat. Mater.* **22** 696–702
[101] Kraus H *et al* 2017 *Nano Lett.* **17** 2865–70
[102] Wang J F, Cui J M, Yan F F, Li Q, Cheng Z D, Liu Z H, Lin Z H, Xu J S, Li C F and Guo G C 2020 *Phys. Rev. B* **101** 064102
[103] Dréau A, Lesik M, Rondin L, Spinicelli P, Arcizet O, Roch J F and Jacques V 2011 *Phys. Rev. B* **84** 195204
[104] Inam F A and Castelletto S 2023 *Nanomaterials* **13** 195
[105] Purcell E M 1995 Spontaneous emission probabilities at radio frequencies *Confined Electrons and Photons: New Physics and Applications* (Springer) pp 839–839
[106] Bekker C *et al* 2023 *Appl. Phys. Lett.* **122** 173507
[107] Hao Z H *et al* 2024 *ACS Photon.* **11** 4725–32
[108] Radulaski M, Fischer K A, Lagoudakis K G, Zhang J L and Vučković J 2017 *Phys. Rev. A* **96** 011801
[109] Norman V A *et al* 2025 *ACS Photon.* **12** 2604–11
[110] Körber J *et al* 2024 *Nano Lett.* **24** 9289–95
[111] Ahamad M A, Ahmed N, Castelletto S and Inam F A 2024 *J. Lightwave Technol.* **42** 689–95
[112] Castelletto S *et al* 2019 *Beilstein J. Nanotechnol.* **10** 2383–95
[113] Inam F A and Castelletto S 2021 *J. Opt. Soc. Am. B* **38** 3697–704
[114] Inam F A and Castelletto S 2021 *J. Appl. Phys.* **130** 083102
[115] Zhou J Y *et al* 2023 *Nano Lett.* **23** 4334–43
[116] Hu Q C, Xu J, Luo Q Y, Hu H B, Guo P J, Liu C Y, Zhao S, Zhou Y and Wang J F 2024 *Opt. Lett.* **49** 2966–9
[117] Dietz J R and Hu E L 2022 *Appl. Phys. Lett.* **120** 184001
[118] Majety S, Norman V A, Li L, Bell M, Saha P and Radulaski M 2021 *J. Phys. Photon.* **3** 034008
[119] Krumrein M *et al* 2024 *ACS Photon.* **11** 2160–70
[120] Hu H *et al* 2024 *Nat. Commun.* **15** 10256
[121] Pelton M 2015 *Nat. Photon.* **9** 427–35
[122] Crook A L *et al* 2020 *Nano Lett.* **20** 3427–34
[123] Lukin D M *et al* 2023 *Phys. Rev. X* **13** 011005
[124] Hessenauer J, Körber J, Ghezellou M, Ul-Hassan J, Astakhov G V, Knolle W, Wrachtrup J and Hunger D 2025 *Opt. Quantum* **3** 175–81
[125] Bulu I, Babinec T, Hausmann B, Choy J T and Loncar M 2011 *Opt. Express* **19** 5268–76
[126] Karamlou A, Trusheim M E and Englund D 2018 *Opt. Express* **26** 3341–52
[127] So J P, Luo J, Choi J, McCullian B and Fuchs G D 2024 *Nano Lett.* **24** 11669–75
[128] Bao T *et al* 2025 *ACS Photon.* **12** 2988–96
[129] Calusine G, Politi A and Awschalom D D 2016 *Phys. Rev. Appl.* **6** 014019
[130] Clevenson H, Trusheim M E, Teale C, Schröder T, Braje D and Englund D 2015 *Nat. Phys.* **11** 393–7
[131] Wang R, Li J, Cai L and Li Q 2023 *Opt. Lett.* **48** 1482–5
[132] Wang R, Li J and Li Q 2025 Optimizing electro-optic modulators for interfacing color centers in an integrated silicon carbide platform (arXiv:2501.16556)
[133] Biagioni P, Huang J S and Hecht B 2012 *Rep. Prog. Phys.* **75** 024402
[134] Hsu C W, Zhen B, Stone A D, Joannopoulos J D and Soljačić M 2016 *Nat. Rev. Mater.* **1** 1–13
[135] Bar-David J, Wolf S A, Indukuri S R K C, Malkinson R, Mazurski N, Levy U and Bar-Gill N 2023 *Phys. Rev. Appl.* **19** 064074
[136] Inam F A, Ahmed N, Steel M J and Castelletto S 2018 *J. Opt. Soc. Am. B* **35** 2153–62
[137] Sortino L *et al* 2024 *Nat. Commun.* **15** 2008

[138] Fisher P, Zappacosta A, Fuhrmann J, Haylock B, Gao W, Nagy R, Jelezko F and Cernansky R 2025 *Nano Lett.* **25** 11626–31
[139] Chen X *et al* 2025 *Adv. Funct. Mater.* **35** 2413529
[140] Fescenko I, Jarmola A, Savukov I, Kehayias P, Smits J, Damron J, Ristoff N, Mosavian N and Acosta V M 2020 *Phys. Rev. Res.* **2** 023394
[141] Seo H, Falk A L, Klimov P V, Miao K C, Galli G and Awschalom D D 2016 *Nat. Commun.* **7** 12935
[142] Cai L, Li J, Wang R and Li Q 2022 *Photon. Res.* **10** 870–6
[143] Bozhevolnyi S I and Khurgin J B 2016 *Optica* **3** 1418–21